Arctic Cloud Response to a Perturbation in Sea Ice Concentration: The North Water Polynya

Emily Monroe[1], Patrick C. Taylor[2], and Linette N. Boisvert[3]

[1]Science Systems and Applications Inc., Hampton, VA

[2]NASA Langley Research Center, Hampton, VA

[3]NASA Goddard Space Flight Center, MD

Corresponding author: Emily Monroe (emily.e.monroe@nasa.gov)

Key Messages:

- Low-cloud cover (< 3 km) is 10-33% larger over the open polynya than adjacent sea ice.
- Cloud radiative effect is 18 W m^{-2} larger over the polynya than nearby sea ice during the event.
- Cloud amount and liquid water content are elevated following closure due to increased moisture fluxes and shifting meteorological conditions.

Abstract

Surface and atmosphere energy exchanges play an important role in the Arctic climate system by influencing the lower atmospheric stability and humidity, sea ice melt and growth, and surface temperature. Sea ice significantly alters the character of these energy exchanges relative to ice-free ocean. The observed decline in Arctic sea ice since 1979 motivates questions related to the evolving role of surface-atmosphere coupling and potential feedbacks on the Arctic system. Due to the strong wintertime cloud warming effect, a critical question concerns the potential response of low clouds to Arctic sea ice decline. Previous approaches relied on interannual variability to investigate the cloud response to sea ice decline. However, the covariation between atmospheric conditions and sea ice makes it difficult to define an observational control when using interannual variability. To circumvent this difficulty, we exploit the recurring North Water (NoW) polynya, an episodic opening in the northern Baffin Bay sea ice, as a natural laboratory to isolate the cloud response to a rapid, near-step perturbation in sea ice. Our results show that during the event (1) low-cloud cover is 10-33% larger over the polynya than nearby sea ice, (2) cloud liquid water content is up to 400% larger over the polynya than nearby sea ice, and (3) the surface cloud radiative effect is 18 W m^{-2} larger over the polynya than nearby sea ice. Our results provide evidence that the low-cloud response during a polynya is a positive feedback lengthening the event.

1 Introduction

Surface-atmosphere interactions strongly influence the character and evolution of the Arctic climate system. The exchange of energy between the surface and atmosphere can generate small- and large-scale atmospheric circulation responses (e.g., Burt et al., 2016; Cohen et al., 2014), warm and moisten the lower Arctic atmosphere (e.g. Screen & Simmonds, 2010; Serreze et al., 2009), influence cloud properties and feedbacks (Kay & Gettelman, 2009; Morrison et al., 2018; Tan & Storelvmo, 2019; Taylor et al., 2015; Vavrus et al., 2004; Zhang et al., 2018), and alter the surface energy budget (Hegyi & Taylor, 2018; Miller et al., 2017). The presence or absence of sea ice introduces a substantial perturbation to surface-atmosphere energy exchanges, and given the observed declines in Arctic sea ice (e.g. Parkinson et al., 2016; Screen & Simmonds, 2010; Simmonds, 2015; Taylor et al., 2018), understanding the effect of varying sea ice cover on surface-atmosphere interactions is an important consideration for understanding the Arctic climate system and modeling its evolution in response to natural variability and anthropogenically-forced climate change.

Sea ice is an efficient insulator that suppresses interaction between the Arctic Ocean and overlying atmosphere. The fluxes of heat and moisture between sea ice and the atmosphere are much smaller and are generally in the opposite direction of energy exchanges between ocean and atmosphere (Gultepe et al., 2003; Taylor et al., 2018). Surface-atmosphere energy exchanges in the Arctic are episodic, occurring under distinct atmospheric conditions in part due to the stark surface temperature contrasts between ocean and sea ice surfaces (Taylor et al., 2018) coupled with the advection of air from one surface to another (e.g., Sjöblom et al., 2020; Taylor et al., 2018; Vihma et al., 2014). Given the surface-type dependence of surface-atmosphere energy exchanges,

a continued decline in Arctic sea ice constitutes a potentially significant impact on the Arctic surface energy budget and the rate of future Arctic warming.

Of the many potential responses to reduced Arctic sea ice cover, the modification of the local thermodynamic environment and formation of clouds represents one of the most consequential. Clouds modify the Arctic climate system evolution through cloud-induced turbulent mixing of the lower tropospheric temperature and humidity structure, modulation of the atmospheric radiative heating rate, precipitation and dehydration of the Arctic atmosphere, and alteration of radiative energy fluxes and the surface energy budget (e.g., Curry et al., 1996; Vihma et al., 2014). Thus, a cloud response to a long-term decline in Arctic sea ice, even a small one, has the potential to significantly alter the Arctic surface energy budget, thereby modulating the Arctic surface temperature change and feeding back on the already reduced Arctic sea ice cover.

A recent emphasis has been placed on understanding the nature and magnitude of Arctic low cloud responses to a changing sea ice cover using internal variability and the seasonal coevolution of Arctic sea ice and clouds (Alkama et al. 2020; Kay & Gettelman, 2009; Morrison et al., 2018; Palm et al., 2010; Taylor et al., 2015; Yu et al., 2019). However, disentangling the influence of covarying meteorology and surface properties on cloud properties and radiative effects from the effects of sea ice is difficult using this approach (Alkama et al. 2020). Studies have addressed this issue by stratifying data into atmospheric regimes (e.g. Barton et al., 2012; Taylor et al., 2015); however, these approaches suffer from the necessary reliance on meteorological reanalyses, which perform poorly at high latitudes (e.g., Cullather et al., 2017; Lindsay et al., 2014). In sum, these results point to a negligible cloud response to the observed summer decline in Arctic sea ice, attributed to the frequent decoupling of clouds from the Arctic surface (Kay & Gettelman, 2009; Morrison et al., 2018; Shupe et al., 2013; Sotiropoulou et al., 2016; Taylor et al., 2015).

Alternatively, a considerable response in cloud amount and cloud liquid water content is suggested during the fall and early winter (Barton et al., 2012; Kay & Gettelman, 2009; Morrison et al., 2018; Taylor et al., 2015). These approaches rely on interannual variations in sea ice cover and atmospheric state to isolate a small but impactful signal from the background noise. Implicit in the reliance on internal variability, however, is the absence of a control cloud state without surface-atmosphere interaction, as the atmosphere, sea ice, and ocean are coupled and continually interact. In this study, we exploit the periodic opening and closing of the North Water polynya (NoW; April et al, 2019; Barber et al., 2001; Vincent, 2019) as a natural laboratory to assess the cloud response to a rapid, near-step change in sea ice cover, relative to the much longer timescale associated with seasonal changes to sea ice cover.

Polynyas are defined as large areas of low sea ice concentration or ice-free ocean when, climatologically, a contiguous ice pack is expected. They represent a sizeable surface energy budget perturbation in the winter and early spring specifically with respect to surface turbulent fluxes (Gultepe et al., 2003; Kottmeier & Engelbart, 1992; Smith et al., 1990). Though strongly impacted by the specific surface and environmental conditions, instantaneous latent and sensible heat fluxes during polynyas often exceed +200 W m^{-2} (e.g. Renfrew et al., 2002; Roberts et al., 2001; Smith et al., 1983; Steffen, 1986). The atmosphere above a polynya becomes warmer and moister, modifying mesoscale atmospheric processes and motions (e.g. Kottmeier & Engelbart, 1992; Walter, 1989), and enhancing surface buoyancy. Polynyas also create conditions conducive for cloud formation that further alter the surface radiative fluxes and can aid in maintaining or expanding the polynya opening (Morales Maqueda et al., 2004; Smith et al., 1990).

In this analysis, we leverage the rapid, near-step change in sea ice cover associated with the NoW polynya to isolate the cloud response under near-constant large-scale meteorological conditions and test three hypotheses:

- There is a statistically significant cloud response to a polynya event where low-cloud amount and liquid water content are larger over the polynya than nearby sea ice;
- The polynya-induced cloud response yields a surface gain of longwave radiation attributable to cloud radiative effects; and,
- Cloud amount and total water content linger for the 8-day period after polynya closure, driven by the polynya perturbation as well as shifting meteorology.

By comparing the average cloud properties before and after a polynya event and exploiting the local gradient in sea ice cover during an event, we provide evidence for a strong cloud response to the polynya opening and show that the interrelated cloud radiative effect serves as a positive feedback lengthening the perturbation.

2 Domain, Data, and Methodology

2.1 North Water (NoW) Polynya

The NoW polynya is a climatological feature located within northern Baffin Bay in Smith Sound east of Ellesmere Island—between approximately 72 and 78°N latitude and 280 to 295°E longitude. The NoW polynya typically opens four to five times between December and March and is associated with the formation of an ice arch in Smith Sound that restricts the flow of sea ice through Kennedy Channel, and the onset of persistent northeasterly winds advecting sea ice and subsequent frazil away from the seasonal ice arch (e.g., Dunbar & Dunbar, 1972; Ito, 1982; Steffen & Ohmura, 1985). Though formed and largely dominated by latent heat polynya processes, Steffen

(1985) posited that northerly winds also induce regions of upwelling near Cape Alexander that bring warm water in contact with cold Arctic air and frazil ice. This results in polynya growth and maintenance of the opening closer to the Greenland coast through sensible heat exchange, especially in late spring (Mysak & Huang, 1992; Steffen & Ohmura, 1985). Thus, latent and sensible heat flux mechanisms play an important role in the onset and lifetime of the NoW polynya (e.g., Barber et al., 2001; Melling et al., 2001).

Table 1 summarizes the areal extent and date range for each polynya event between December 2006 and March 2010, determined using passive microwave sea ice concentration (SIC; Cavalieri et al., 1996). Consistent with Boisvert et al. (2012), a NoW polynya event is defined as the dates during which average SIC within the region (polar stereographic square bounded by northwest point 76.95°N, 265°E and southeast point 74.4°N, 305.5°E) falls below 85%; the closure date is the next date that the average SIC for the region exceeds 85%. The NoW Polynya area is computed using a SIC threshold of 60%. NoW polynyas between 2006 and 2010 had an average areal extent of 17,461 ± 11,668 km^2 and an average length of 8.44 ± 2.40 days.

Table 1. Summary of polynya events. The calculation of average area uses footprints with SIC <60% to define the polynya (NSIDC).

#	START	END	# DAYS	AVG AREA (km^2)
1	20070111	20070120	10	6 063
2	20070127	20070201	6	25 313
3	20070205	20070215	11	35 170
4	20070307	20070311	5	6 125
5	20071211	20071216	6	29 792
6	20080118	20080128	11	13 352
7	20080219	20080225	7	5 179
8	20080304	20080309	6	833
9	20081202	20081207	6	18 854
10	20090120	20090130	11	12 386
11	20090314	20090324	11	12 784
12	20091210	20091220	11	42 500
13	20091222	20091226	5	24 750
14	20100120	20100128	9	14 444
15	20100131	20100208	9	26 041
16	20100316	20100326	11	5 795
AVERAGE			8.44	17 461

147

148

149

150 2.2 CALIPSO-CloudSat-CERES-MODIS (C3M) Data

151 The Cloud-Aerosol Lidar and Infrared Pathfinder Satellite Observation (CALIPSO)-CloudSat-
152 Clouds and the Earth's Radiant Energy System (CERES)-Moderate Resolution Imaging
153 Spectrometer (MODIS) (C3M) data fusion product extends from July 2006 to June 2010 (Kato et
154 al., 2010, 2011). C3M provides vertically resolved profiles of cloud fraction (CF), liquid water
155 content (LWC), and ice water content (IWC) with computed top-of-atmosphere, in-atmosphere,
156 and surface radiative fluxes. Data are aggregated along 20 km nadir ground track segments
157 collocated with the CERES footprint. C3M includes auxiliary temperature and humidity profile
158 data from Global Modeling and Assimilation Office GEOS-4 before Nov. 2007 and GEOS-5 after.
159 Kato et al. (2010) provide a complete description of the data fusion process.

160 CALIPSO and CloudSat active remote sensing observations provide vertically resolved cloud
161 properties and offer distinct advantages over passive remote sensing techniques. During polar
162 night, passive remote sensing retrievals exhibit large uncertainties due to the necessary reliance on
163 a few thermal emission channels (e.g., Minnis et al. 2011b). Vertically resolved cloud properties
164 from CALIPSO-CloudSAT measurements provide critical information to characterize the
165 response of clouds to polynya events. Uncertainty in C3M cloud fraction is considered to be small
166 (~0.01) as CALIPSO is extremely sensitive to cloud condensate (e.g., Avery et al., 2012). Cloud
167 LWC and IWC are determined by joining CALIPSO and CloudSat measurements with MODIS
168 cloud optical depth retrievals using the CERES science team Edition 3 retrieval algorithms defined
169 by Minnis et al. (2011a, 2011b). Currently, *in situ* observations of Arctic low cloud LWC and IWC
170 over sea ice are rare and rigorous uncertainty estimates are unavailable. We adopt uncertainties of
171 ±20% for LWC, ±70% for IWC, and ±2K for surface temperature (Henderson et al. 2013).

2.3 Surface Turbulent Flux data

Surface turbulent flux data are taken from three sources: (1) a satellite-derived data set using the NASA Atmospheric Infrared Sounder (AIRS) temperature and humidity retrievals (Boisvert et al., 2013), (2) the Modern-Era Retrospective analysis for Research and Applications, Version 2 (MERRA-2; Gelaro et al., 2017), and (3) the ECMWF Re-Analysis, fifth generation (ERA5; Hersbach et al. 2018). The AIRS-based surface turbulent flux retrieval technique applies bulk aerodynamic formulae using stability effects corresponding to the Monin-Obukhov similarity theory to calculate sensible and latent heat fluxes from AIRS-retrieved surface skin and near-surface (1000 hPa) temperature, specific humidity, and geopotential height (Boisvert et al., 2013). This method uses an iterative approach consistent with Launianinen and Vihma (1990) and additional modifications applying the Grachev et al. (2007) flux algorithm for stable conditions and roughness length estimates over sea ice following Andreas et al. (2010a, 2010b). Iterative methods enable the use of air temperature and specific humidity measured at varying heights, interpolated to a 2-m reference height. The method applies different bulk formulae over sea ice and water and then uses passive microwave SIC as a weight to compute the daily averaged sensible heat (SH) and latent heat (LH) fluxes for a 625 km^2 pixel on a polar stereographic grid.

Boisvert et al. (2012) use this AIRS-based surface turbulent flux data set to study the progression of moisture fluxes over the NoW polynya, showing event-integrated moisture fluxes in agreement with previous studies and a ±25% uncertainty. Taylor et al. (2018) showed comparisons between *in situ* buoy measurements observed during the N-ICE2015 campaign and corresponding AIRS-based surface turbulent flux data, reporting a bias of -0.49 W m^{-2} and root mean square error of 0.74 W m^{-2} for LH and a bias of +0.11 W m^{-2} and root mean square error of 5.32 W m^{-2} for SH. The N-ICE2015 campaign occurred in a different synoptic environment and

surface conditions than the North Water polynya. This may impact the representativeness of the estimated surface turbulent flux uncertainty from the N-ICE2015 data to the NoW region; however, parallels can be drawn between the present study and the sea ice environment (dynamic, young first year ice) and season (winter) in which N-ICE2015 data was collected. Despite the small validation sample size, these results highlight a strong correspondence between *in situ* observations and satellite retrieved surface turbulent fluxes, allowing for greater confidence in the usage of AIRS-based analyses.

The MERRA-2 surface turbulent fluxes are directly output from the data assimilation system. MERRA-2 employs an updated 3D-variational assimilation system with incremental analysis updates and has a comparable cubed-sphere grid with spacing of ½° (69 km) (Bosilovich et al., 2016; Molod et al., 2015). The surface turbulent fluxes are computed via the Monin-Obukov similarity theory and based on an analysis methodology described in Helfand & Schubert (1995). The parameterizations for the boundary layer and surface roughness employed in this scheme are meant for land surfaces only, with no changes made for fluxes produced over sea ice.

Sea ice concentrations use the daily SST product of Reynolds et al. (2007) until April 2006 and then the Operational Sea Surface Temperature and Sea Ice Analysis (OSTIA) product (Donlon et al., 2012) thereafter. The sea ice representation can be described as simple, with sea ice represented as a uniform 7-cm skin layer slab with no snow cover and is subsequently used in surface energy budget calculations to determine the skin temperature (Bosilovich et al. 2015). Arctic sea ice thickness and snow cover are highly variable, however, and the use of a uniform slab negatively affects surface temperature estimates as more heat is conducted through the slab than in reality, leading to warm temperature biases particularly in winter months.

ERA5 is an updated version of ECMWF's ERA-Interim which offers a higher spatial and temporal resolution. ERA5 has hourly data with a horizontal resolution of 31 km. Like ERA-Interim, it uses a 4-D variational assimilation scheme (Hersbach et al., 2016). The turbulent fluxes are estimated via the Monin-Obukov Similarity Theory, which is described in detail in the ISF Documentation (Cy41r2, 2016). ERA5 uses the same stability functions globally, with no changes made to the scheme in the Arctic (IFS Documentation–Cy41r21, 2016). While this scheme works well for the midlatitudes, it may not work well over the Arctic sea ice. For the stable boundary layer, ERA5 uses parameterizations from Holtslag and De Bruin (1988). This parameterization was produced using stable nocturnal boundary layer data over land, and is not designed to reproduce the stable boundary layers over sea ice. ERA5 also uses constant roughness lengths for heat and moisture over sea ice; however, the roughness of sea ice varies both spatially and temporally (Andreas et al., 2010a, 2010b).

Until August 2007, ERA5 utilizes the Hadley Center sea ice and sea-surface temperature data set version 2 (HadISST2; Titchner & Rayner, 2014) and OSI-SAF reprocessing for daily sea ice concentration (Eastwood et al., 2014). Beginning in September 2007, ERA5 uses the OSI-SAF daily sea ice and OSTIA (Donlon et al., 2012). Sea ice is simplified in ERA5 like in MERRA-2. Here the sea ice is a fixed depth slab with a fixed sea ice fraction, and there is no snow accumulation on top of the ice (ISF Documentation – Cy41r2, 2016).

In comparison with N-ICE *in situ* observations, Graham et al. (2019) found that the sensible and latent heat fluxes are simulated poorly by MERRA-2 and ERA5 and tend to be in the opposite direction of observed fluxes. The sensible heat flux from MERRA-2 was found to have a large RMSE of 38 W m^{-2}, a -5 W m^{-2} bias in latent heat, and also a warm and moist bias near the surface (Graham et al., 2019). ERA5 was found to have a 32 W m^{-2} RMSE in sensible heat flux and

a -3 W m^{-2} bias in the latent heat flux, and one of the largest temperature biases compared to the other reanalysis in the wintertime (Graham et al., 2019). The fraction of open water in the grid cells is likely a substantial contributing factor to the large biases in the turbulent fluxes from these reanalyses in the wintertime over sea ice. Conversely, AIRS-derived sensible and latent heat fluxes had RMSEs of ~5 and ~1 W m^{-2} when compared with the N-ICE data (Taylor et al., 2018).

Since the sea ice and subsequent snow cover on sea ice is highly variable both spatially and temporally (Kwok et al., 2017; Wang et al., 2016) and both MERRA-2 and ERA5 have a simplified sea ice representation, the skin temperature and surface fluxes are likely to be negatively affected in both of the reanalysis products.

2.4 Compositing Methodology: A phenomenological compositing approach

Our methodology exploits the rapid near-step perturbation and natural gradients in SIC during NoW polynya openings to define an experimental control, such that meteorology can be treated as constant and the effects of surface type can be assessed. The ultimate goal is to isolate the cloud response that results from surface type differences alone. Applying a phenomenological compositing approach, we compile C3M footprints from CALIPSO-CloudSat ground tracks that cross both the polynya and nearby sea ice. Individual footprints are defined as either "polynya" or "ice": polynya footprints are those with SIC< 60%, considered to be within the polynya (water footprints adjacent to land are omitted), and ice footprints are those with SIC $\geq$85%. Only overpasses that intersect both polynya and ice footprints are considered. An impediment to this approach is that the nadir-only CALIPSO-CloudSat sampling limits the data captured during each polynya event and additional constraining of the data further reduces the sample size. The SIC thresholds for the two subgroups (polynya and ice) are disjoint in an effort to more effectively detect a polynya signal relative to noise and to mitigate the influence of any polynya-scale

263 atmospheric circulation response. The 60% SIC threshold is selected to balance the number of
264 samples and the cloud response signal. The sensitivity of our results to the SIC threshold was tested
265 using SIC values between 30% and 85% and showed a consistency of the overall results across all
266 thresholds.

267 Figure 1 shows an example of three overpasses of the NoW polynya on March 19, 2009, one
268 of which intersects the polynya and meets the stated criteria. Though all three tracks provide data
269 within the region, only water (blue) and ice (cyan) points from the central track extending from
270 northwest to southeast are included in the analysis. In total, data are aggregated over 16 polynya
271 events yielding 145 polynya points and 280 ice points.

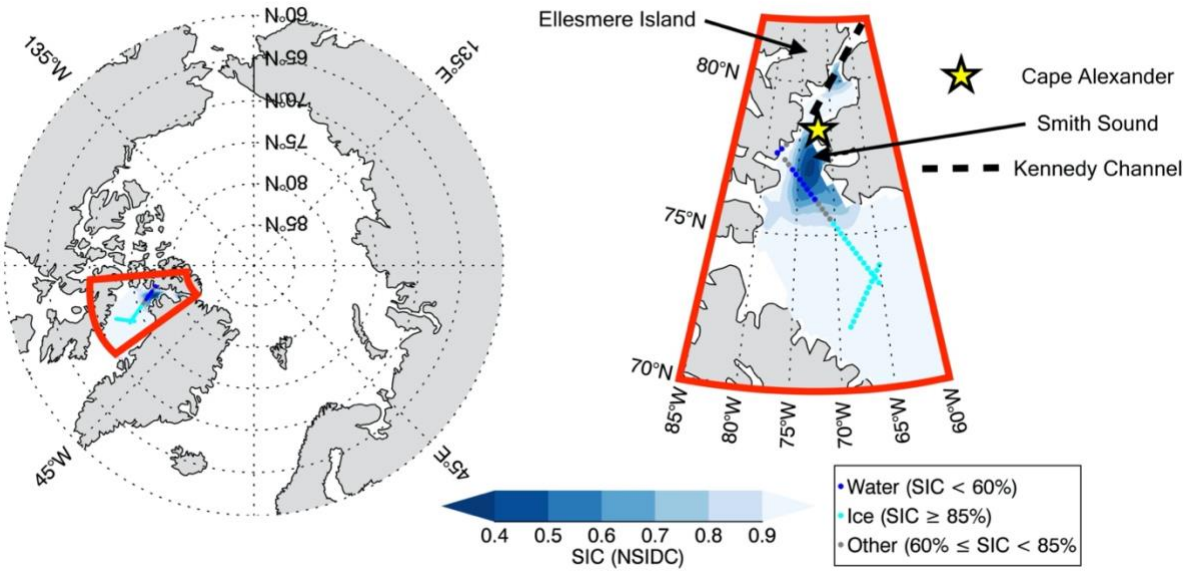

272

273

274 **Figure 1.** Sample image showing C3M satellite ground track through the region (points) overlayed
275 on the NSIDC SIC data (contours). Footprints are stratified by surface type using SIC with those
276 <60% SIC categorized as "water" (blue), those ≥85% categorized as "ice" (cyan) and remaining

277 points categorized as "other" and unused (grey). The filtered swath approach means that only water
278 and ice points along the C3M ground track oriented in the northwest-southeast direction are used.
279

280 **3 Results**

281 3.1 Surface-type dependence of cloud property vertical profiles

282 Figure 2 depicts the average CF vertical profiles for polynya and ice footprints composited
283 over all events. The average CF profiles for each surface type exhibit similar shapes and increase
284 from the surface to ~600-700 m, hereafter denoted as the level of maximum (LoM) CF, after which
285 CF decreases approaching a near-constant value above ~2.2 km (Fig. 2a). The hashed and dotted
286 lines mark the 1-σ uncertainty intervals over each surface type (Fig. 2a). Differences between the
287 two surface types (Fig. 2b) show that the average CF profile is larger over the polynya than that
288 over nearby ice, and statistically significant (95% confidence, $p < 0.05$) differences range from
289 0.05 to 0.33. The largest CF differences occur between 700 and 1100 m and correspond to the
290 LoM CF over each surface type. CF differences become statistically insignificant above 2.2 km
291 indicating that the polynya-induced cloud response is confined below this altitude.

292 Mean LWC profiles for polynya and ice footprints (Fig. 2c) differ dramatically, with
293 statistically significant differences found between the profiles. LWC over ice footprints shows a
294 bottom-heavy profile with maximum values in the lowest 200 m, whereas LWC increases swiftly
295 with height over polynya footprints reaching a maximum at ~600 m. LWC over polynya footprints
296 is substantially larger than that over nearby ice between 200 and 900 m with differences exceeding
297 100%. The largest differences, measured to be ~400% higher over polynya than over ice, coincide
298 with the LWC maximum over polynya footprints reaching 0.026 g m^{-3} near 600 m (Fig. 2c, 2d).

299 The LWC differences decrease more rapidly with height than CF and approach zero near 1.3 km
300 (Fig. 2c).

301 The percent differences between average IWC profiles for the polynya and ice footprints are
302 smaller than for the LWC profiles. While not statistically significant, this response is consistent
303 with the presence of abundant cloud condensation nuclei and fewer ice nucleating particles. The
304 average IWC profiles for the two surface types increase with height above the surface and reach a
305 broad maximum between 700 m and 1.3 km (Fig. 2e). Figure 2f indicates the largest differences
306 between the IWC profiles occur in the 1.0 to 1.3 km altitude range, with IWC over polynya ~0.05
307 g m^{-3} larger than over ice, a near-doubling of IWC relative to ice footprints.
308

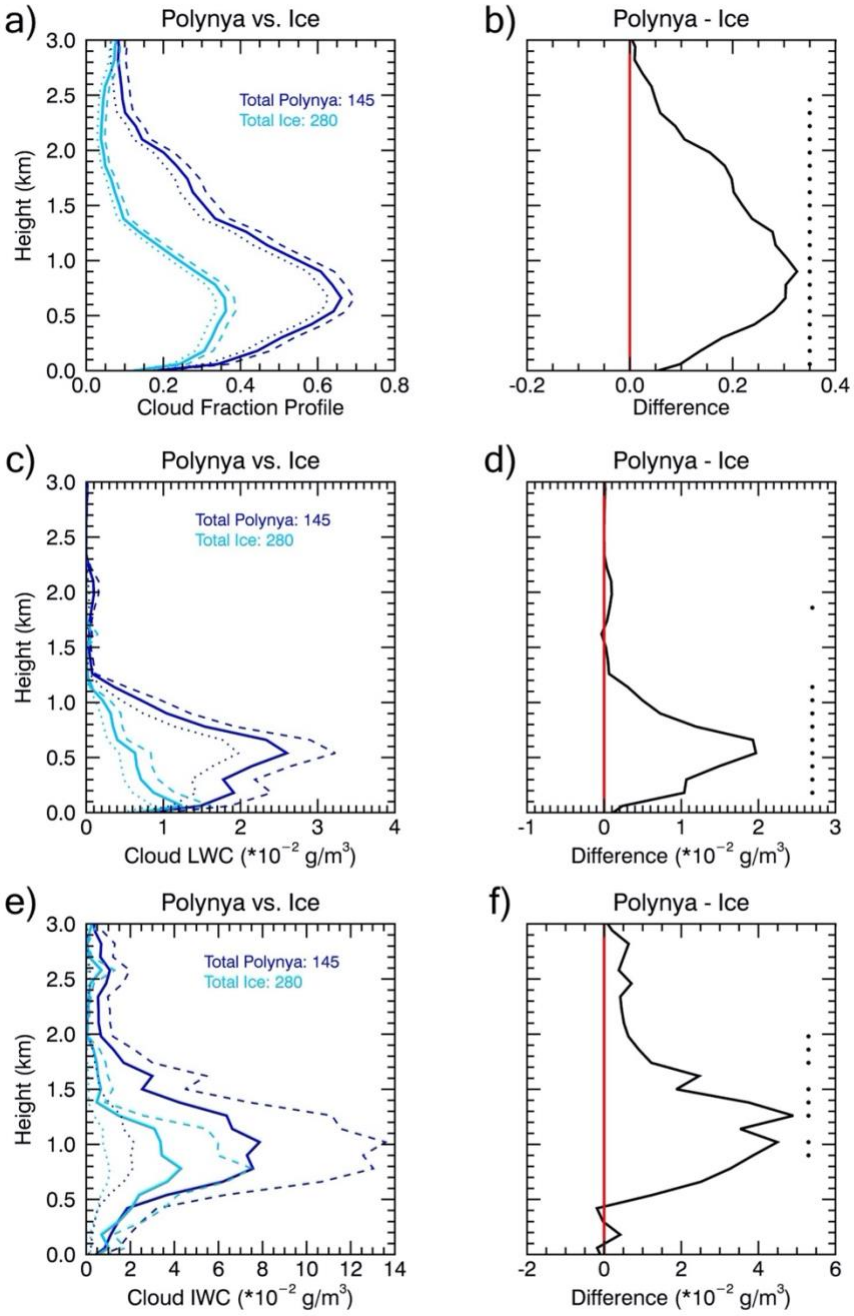

Figure 2. The average vertical profiles and differences by surface type are shown for (a,b) cloud fraction (CF), (c,d) liquid water content (LWC), and (e,f) ice water content (IWC) using filtered swaths from ice (SIC ≥ 85%, light blue), and polynya (SIC <60%, dark blue) footprints for 0-3 km (solid). Hashed lines (mean + combined uncertainty) and dotted lines (mean – combined uncertainty) represent the range of ±1σ uncertainty. The vertical dots on the right hand side of each

difference panel represent vertical levels where $p < 0.05$ as determined by a Students-t difference of means test between the surface types.

3.2 Distribution of cloud variable differences over polynya and ice

Based on the average cloud property profiles, Section 3.1 indicates that surface type influences cloud properties across the NoW polynya. An additional approach is to compute the near-instantaneous, single-track differences between polynya and ice footprints (Fig. 3). This method resembles the approach employed in airborne campaigns (e.g., Smith et al., 2017) to sample cloud properties over polynya and ice under similar large-scale meteorological conditions. Applying this approach to satellite data provides a characterization of the surface type influences over the course of a few seconds compared to a few hours. To apply this approach, we further subset satellite tracks to include only those with two or more consecutive footprints of each surface type, yielding 25 tracks. While sampling is a clear limitation, the lack of meaningful large-scale meteorological changes over the course of ~10 seconds is an advantage.

Figure 3 shows the frequency distribution of near-instantaneous cloud property differences between polynya and ice surfaces at three vertical levels: near-surface (180-300 m), LoM CF (540-660 m), and above LoM CF (1.25-1.38 km). The difference in single-track CF between polynya and ice (0.43) is largest at the LoM CF; however, the distribution of single-track differences appears bimodal with frequency peaks near 0.25 and 0.5 (Fig. 3d). Above the LoM CF, the mean difference is less (0.32; Fig. 3a) and more than half of the calculated differences are less than the mean difference, with values near 0.25. This is also the bin with the largest frequency for the LoM CF. Closer to the surface, the mean difference is similar (0.32) and the distribution skews towards more frequent differences smaller than the mean (the largest bin shows >30% of differences are

~0.1; Fig. 3g), while the range of differences is broad (0.1 to 0.75). It is important to note that the mean differences shown in Fig. 3 are greater than those shown in Fig. 2b for all three levels.

Surface-type differences for LWC (Fig. 3b, 3e, 3h) are also greater than the mean differences (Fig. 2d) at all three levels. The distribution of LWC at the LoM CF is broader than for CF and the differences resemble a uniform distribution between 0.020 and 0.033 g m^{-3} (Fig. 3e). Above the LoM CF, the mean difference is three orders of magnitude smaller than that observed at the LoM CF and >65% of tracks show a difference of zero (Fig. 3b), indicating that the LWC response is confined below this level. The near-surface layer shows differences mostly between 0.01 and 0.025 g m^{-3} (>70% of samples) and a few instances of differences >0.04 g m^{-3} (Fig. 3h).

Turning to IWC, though the overall largest differences are observed at the LoM CF (~10% of samples have a difference greater than 0.11 g m^{-3}), the distribution is highly skewed with over 50% of samples showing differences less than ~0.01 g m^{-3} (Fig. 3f). The mean difference in IWC at the LoM CF is 0.034 g m^{-3}, slightly less than the layer above where the mean difference is 0.038 g m^{-3} (Fig. 3c). At the level above LoM CF, the distribution is broader and more uniform with no bin showing a frequency >0.2. In the near-surface layer, IWC differences span -0.025 to 0.035 g m^{-3} with the maximum centered on zero (nearly 80% of samples between -0.005 and 0.005 g m^{-3}) and long tails of sparse representation extending in both the positive and negative directions (Fig. 3i).

In summary, despite sample size limitations the results indicate that CF, LWC, and IWC are greater over polynya than over ice, consistent with Section 3.1.

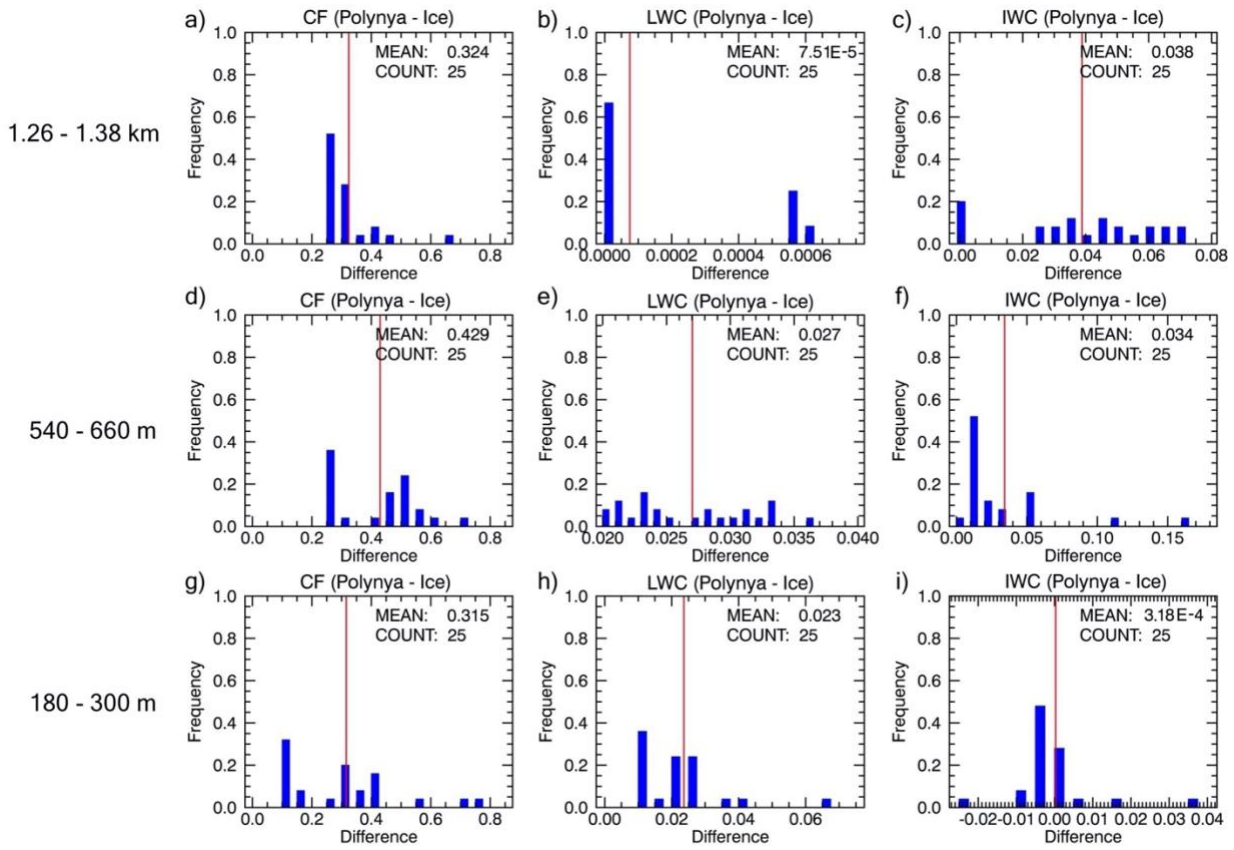

Figure 3. Probability density functions displaying frequencies of same-swath differences across three layers above (a-c; 1.26-1.38 km), near (d-f; 540-660 m) and below (g-i; 180-300 m) the level where maximum CF is reached during an average polynya event. Differences are calculated for CF (left column), LWC (center column), and IWC (right column) over the polynya versus over the ice (i.e. polynya – ice). Averages are represented by the vertical red line.

3.3 Cloud radiative response and regional surface energy budget evolution

Table 2 summarizes the NoW regional (72-78°N and 280-295°E) surface energy budget evolution before, during, and after the polynya. Average fluxes for the paired before and after periods are computed as the 8-day regional average, selected to be consistent with the average polynya length. In cases where consecutive events are too close to define before and after periods

without overlap, the event was omitted from this analysis. Additionally, events 14 and 15 are treated as a single event as the closing and reopening were separated by 2 days (Table 1).

The smallest regionally averaged radiative fluxes occur before the event, increase once the polynya opens, and continue to increase after the polynya closes (Table 2). Regionally averaged surface upwelling and downwelling longwave (LW) fluxes show statistically significant differences from before to after a polynya event, highlighting their lingering presence and slight enhancement after the polynya closes. Additionally, regional surface temperature remains flat from before to during the event, but increases after the event by 2 K. We speculate that the increased clear-sky downwelling LW flux and surface temperature results from the continued spreading of the warmer, moister air over the polynya to the broader region. It is possible that southerly advection into the region also increases downwelling LW clear-sky fluxes and temperature as the winds shift from being more northerly in the "before" and "during" periods to becoming more southerly "after" (Figs. S1-S3). Recent studies indicate a strong connection between moisture advection from lower latitudes and enhanced LW downwelling fluxes and skin temperature in the Arctic (Lee et al., 2017; Luo et al., 2017) and the Antarctic (Sato et al., 2021). These results suggest that increased moisture advection from lower latitudes could be playing a role in the elevated regional cloudiness after polynya closure. Uncertainty prevents any substantial conclusions between regional radiative observations collected during the event and those collected before or after.

Table 2 also shows differences in the average radiative fluxes, surface temperature, and lower tropospheric stability (LTS) during the event separated by surface type. Whereas NoW regional averages for each time period incorporate all available data, polynya and ice categories only use footprints that meet the orbit qualifications in Section 2, causing the regional averages during the

event to not always fall between polynya and ice surface type averages. The LW upwelling fluxes are ~9-10 W m^{-2} larger over polynya compared to ice footprints, due to a ~2 K warmer surface temperature. LTS over the polynya is weaker relative to that over the ice, reflecting the differences observed between cloud development over each surface type (Fig. 2). All-sky downwelling LW flux differences between polynya and ice footprints are overwhelmingly driven by CRE, in contrast to the regional variations caused by clear-sky flux changes. During the event, polynya footprints show an ~18 W m^{-2} larger LW CRE than nearby ice footprints and a ~2 W m^{-2} larger downwelling LW clear-sky flux. Overall, both polynya and ice footprints show increased LW CRE relative to the regional average before the event; however, the average LW CRE over ice footprints increases by <1 W m^{-2} relative to the before-event regional average while polynya footprints show a ~20 W m^{-2} increase. As a result, the net all-sky LW flux over the polynya is ~6 W m^{-2} less negative than the regional average during the event. Thus, the cloud-response to the polynya induces a nearly ~20 W m^{-2} gradient in the surface energy budget, indicating that clouds slow refreezing and represent a positive feedback on polynya length.

Table 2. Summary of the regional surface energy budget evolution during the NoW polynya. Averaged surface longwave downwelling and upwelling radiation, and latent and sensible heat fluxes over polynya and over ice for eight day paired periods before and after, as well as during the polynya. Values shown are % for SIC, K for temperature and LTS, and in W m^{-2} for all others. Bold values indicate statistical significance with $p < 0.05$ as determined by a Students-t differences of means test, with "before" compared with "after" and "polynya" with "ice". *Standard error is shown for C3M LTS, and MERRA-2 and ERA5 LH and SH due to unclear systematic uncertainty.

	Before (8 day period leading up to event)	**During**			**After (8 day period following event)**
	Box Average (full)	Box Average (full)	Polynya	Ice	Box Average (full)
SIC (NSIDC)	**0.93 (0.05)**	0.88 (0.05)	**0.51 (0.05)**	**0.92 (0.05)**	**0.91 (0.05)**
Temperature (C3M)	**250.3 (2.1)**	250.8 (2.0)	**252.1 (2.1)**	**250.2 (2.0)**	**252.4 (2.1)**
LTS (C3M)	25.2 (0.7*)	27.4 (0.1*)	**26.5 (0.4*)**	**28.9 (0.3*)**	24.4 (0.5*)
Downwelling Longwave					
All-Sky	**179.3 (12.4)**	184.0 (12.0)	**200.8 (12.2)**	**180.3 (12.1)**	**190.4 (12.5)**
Clear-Sky	148.4 (12.2)	151.5 (12.0)	151.1 (12.1)	148.9 (12.0)	154.8 (12.3)
CRE	30.9 (16.1)	32.5 (16.0)	**49.7 (16.1)**	**31.4 (16.1)**	35.6 (16.1)
Upwelling Longwave					
All-Sky	**219.9 (12.2)**	224.9 (12.0)	**235.5 (12.1)**	**226.0 (12.0)**	**229.7 (12.3)**
Clear-Sky	**219.2 (12.2)**	224.2 (12.0)	**234.6 (12.1)**	**225.4 (12.0)**	**229.0 (12.3)**
Net LW radiation	**-40.6**	-40.9	**-34.7**	**-45.7**	**-39.3**
LH (AIRS-based)	0.9 (0.5)	-1.4 (0.3)	**3.4** (1.8)	**-3.1** (0.9)	-1.1 (1.4)
SH (AIRS-based)	-11.5 (3.3)	-21.7 (5.4)	**-1.6** (3.4)	**-29.1** (7.6)	-14.2 (4.2)
LH (MERRA-2)	**18.6 (0.5*)**	24.1 (0.0*)	**50.2** (2.4*)	**12.4** (0.8*)	**20.7 (0.7*)**
SH (MERRA-2)	**48.8 (2.3*)**	58.0 (0.1*)	**103.2** (6.1*)	**25.4** (2.5*)	**49.3 (2.3*)**
LH (ERA5)	**5.3 (0.3*)**	14.8 (0.1*)	**64.1** (3.6*)	**7.2** (0.6*)	**8.0 (0.5*)**
SH (ERA5)	4.3 (0.8*)	18.8 (0.2*)	**118.1** (8.3*)	**1.2** (1.3*)	6.2 (1.4*)

Figure 4 shows scatterplots of event-averaged area and event length compared against average LW CRE to further investigate the relationship between polynya characteristics and the cloud radiative response. Though confidence is limited by sample size, the results suggest that a longer and larger polynya produces a stronger influence on the regional surface energy budget. The polynya area appears to have a stronger influence on the regional energy budget than event length; in particular, the strongest relationship is observed between average area and regionally-averaged CREs after the event (Fig. 4f). Considering more events is needed to expand this analysis.

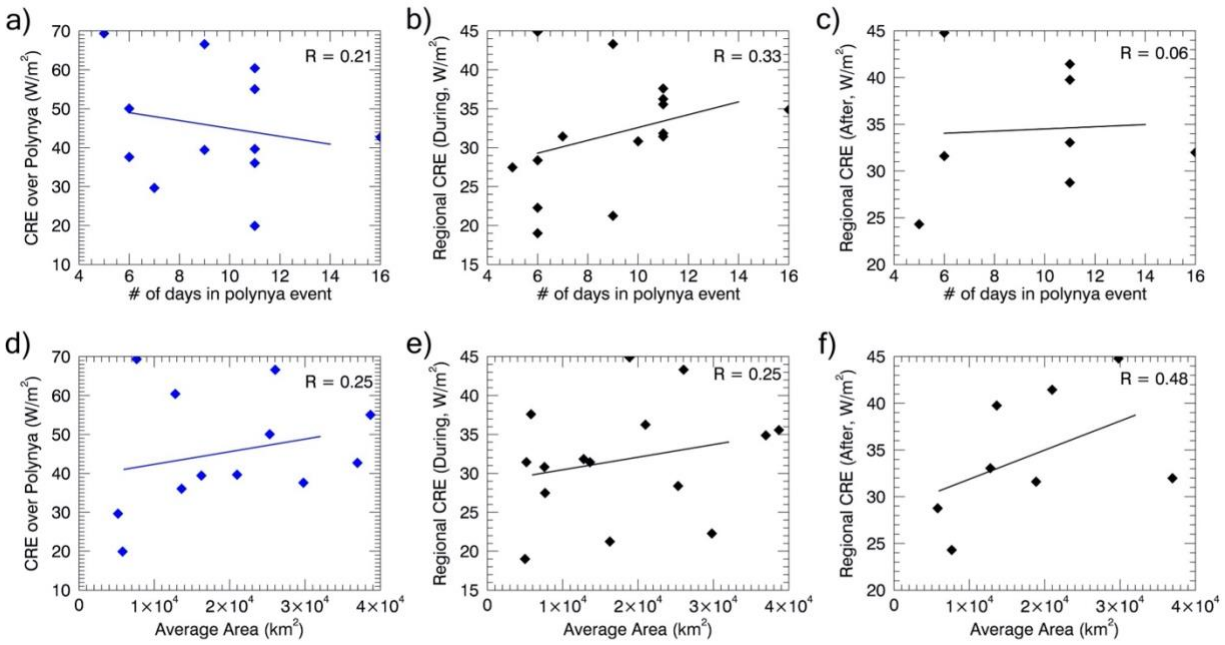

Figure 4. Scatterplots summarizing the relationships between (a,d) over-polynya and (b,e) regionally-averaged CRE during the event, and (c,f) regionally-averaged CRE after the event and the number of days in a polynya event (a, b, c) and average polynya area (d, e, f).

Surface turbulent fluxes also vary strongly across the region during a polynya event. Before the event, regionally averaged LH flux from the AIRS-based data set is near-zero whereas the SH flux is strongly negative (Table 2). During the polynya, regional mean SH and LH fluxes increase towards the surface (negative sign in Table 2) corresponding to the larger increase in the regionally averaged near-surface air temperature and specific humidity than surface temperature and surface saturation specific humidity. Considering the breakdown by surface-type, the LH fluxes over polynya footprints indicate a surface-to-atmosphere transfer of energy (~3 W m^{-2}) whereas there is a net atmosphere-to-surface transfer of energy (~ -3 W m^{-2}) over ice footprints. For SH fluxes, ice footprints show a strong atmosphere-to-surface transfer of energy (~ -29 W m^{-2}) and polynya footprints show a much weaker SH flux (~ -1 to -2 W m^{-2}) indicating a weak difference between

the near-surface air and surface temperature. The regional average SH and LH fluxes after the polynya event are both directed to the surface and in the case of SH more strongly than before, indicating an enhanced near-surface air and surface temperature difference after the event. Overall, the evolution of the surface turbulent fluxes suggest that the polynya warms and moistens the regional atmosphere, enhancing energy transfer from the atmosphere to the surrounding sea ice surface.

MERRA-2 and ERA5 surface turbulent fluxes show dramatic differences with the AIRS-based fluxes. First, the average fluxes across the region are opposite to the AIRS-based fluxes showing positive values before, during, and after the event. MERRA-2 and ERA5 also show a different evolution of SH and LH through the polynya event, suggesting that both LH and SH fluxes support a stronger surface-to-atmosphere transfer of energy on a regionally averaged basis. Comparing the breakdown by surface type shows much larger LH and SH differences between the polynya and ice footprints during the event.

Although available data sources do not provide a consistent picture, consistently positive surface turbulent flux retrievals from MERRA-2 and ERA5 over winter sea ice suggest a poor representation of sea ice and snow cover on sea ice, and subsequent limitations in near-surface estimates of temperature and specific humidity are likely producing skewed surface fluxes. Moreover, the surface turbulent flux evolution found within the satellite data set is consistent with previous studies (Yao & Tang, 2002; Boisvert et al., 2012, 2015, 2020) and is used below in subsequent analysis of the cloud response to the polynya.

3.4 Evolution of regional cloud profiles and surface radiative budget across a polynya event

An additional approach to quantifying the total cloud response to the polynya event is to compare the cloud property profiles before and after the event, constraining data to only include

events that had corresponding uninterrupted before and after periods (as with Table 2). A benefit of this approach is the substantial increase in the number of footprints: 1980 before and 1986 after. Figure 5 shows the regionally averaged CF, LWC, and IWC profiles composited before and after the polynya. Small differences are found in the regionally averaged CF profiles closest to the surface (< 300 m), however statistically significant differences (denoted by the vertical dots in Fig. 5) of 0.05 to 0.09 are found from 300 m up to 3 km (Fig. 5a).

Changes in the regionally averaged LWC profiles indicate similar changes as the CF profiles. Figure 5b shows that all altitudes with statistically significant differences above 500 m correspond to a greater LWC after the polynya than before. Below 500 m, the LoM LWC shifts upward by ~100 m and does not show as sharp a decline in the layer immediately above. The LWC profile after the event indicates that the LoM LWC remains elevated in the 8-day period after closure. We hypothesize that lingering warming and moistening effects from the polynya contribute to the increased LWC. Statistically significant LWC increases of 0.001 to 0.002 g m^{-3} are found between 900 m and 1.4 km, consistent with the largest changes observed in CF. The presence of weak low cloud dissipative mechanisms (e.g. suppressed or no evaporation by boundary layer convective heating, precipitation, or absorption of solar radiation that might exert a greater influence during another season; Herman & Goody, 1976) and the shift to a southerly wind regime (Figs. S1-S3) may also contribute to lingering elevated LWC values. As for IWC, Figure 5c illustrates changes in the regional mean IWC profile broadly suggest a redistribution of IWC from near the surface before the event to higher altitudes after; however, the IWC differences are too uncertain to draw any substantial conclusions.

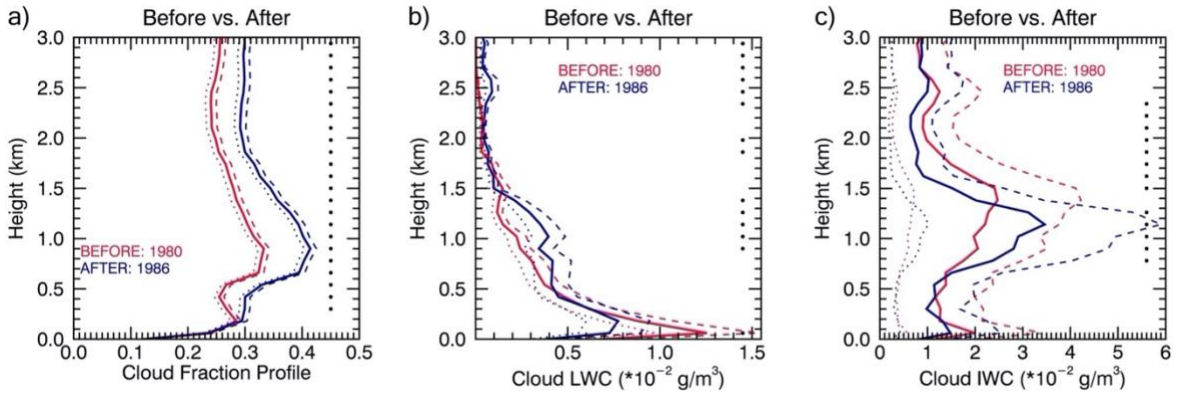

Figure 5. Mean 0-3 km vertical profiles of regionally averaged (a) CF, (b) LWC, and (c) IWC before (red) and after (blue) a polynya event. Hashed lines (mean + combined uncertainty) and dotted lines (mean – combined uncertainty) represent ranges of ±1σ uncertainty. Vertical blue (red) dots in the right of each panel represent vertical levels where the "before" and "after" event differences are statistically significant with $p < 0.05$ as determined by a Students-t difference of means test.

Figure 6 shows the composite time-series of regional mean surface radiative fluxes illustrating the evolution of the polynya signal. Whereas Table 2 features 8-day means, Fig. 6 features centered 5-day running means. Five-day periods were selected instead of the previous 8-day averages as to not over-smooth any signal across the two-week period following the closure. Similar to Table 2, upwelling and downwelling LW fluxes increase with the opening of a polynya and remain elevated after the closure (Fig. 6). Regional fluxes begin to slacken in the period immediately following the closure of the polynya (i.e. days 1-5) as surface turbulent fluxes decrease rapidly. These results indicate the regional influence of the polynya on the surface energy budget is largely confined to the week following the closure. Clouds linger and likely spread out and moisten the region, however the LW CRE shows no statistically significant change. Post-event moisture advection

500 from lower latitudes also likely contributes to the lingering LW downwelling flux (Lee et al., 2017;
501 Luo et al., 2017). After the event, the enhanced upwelling all-sky and clear-sky fluxes immediately
502 following the polynya closure aid in removing the heat and returning the region to normal.

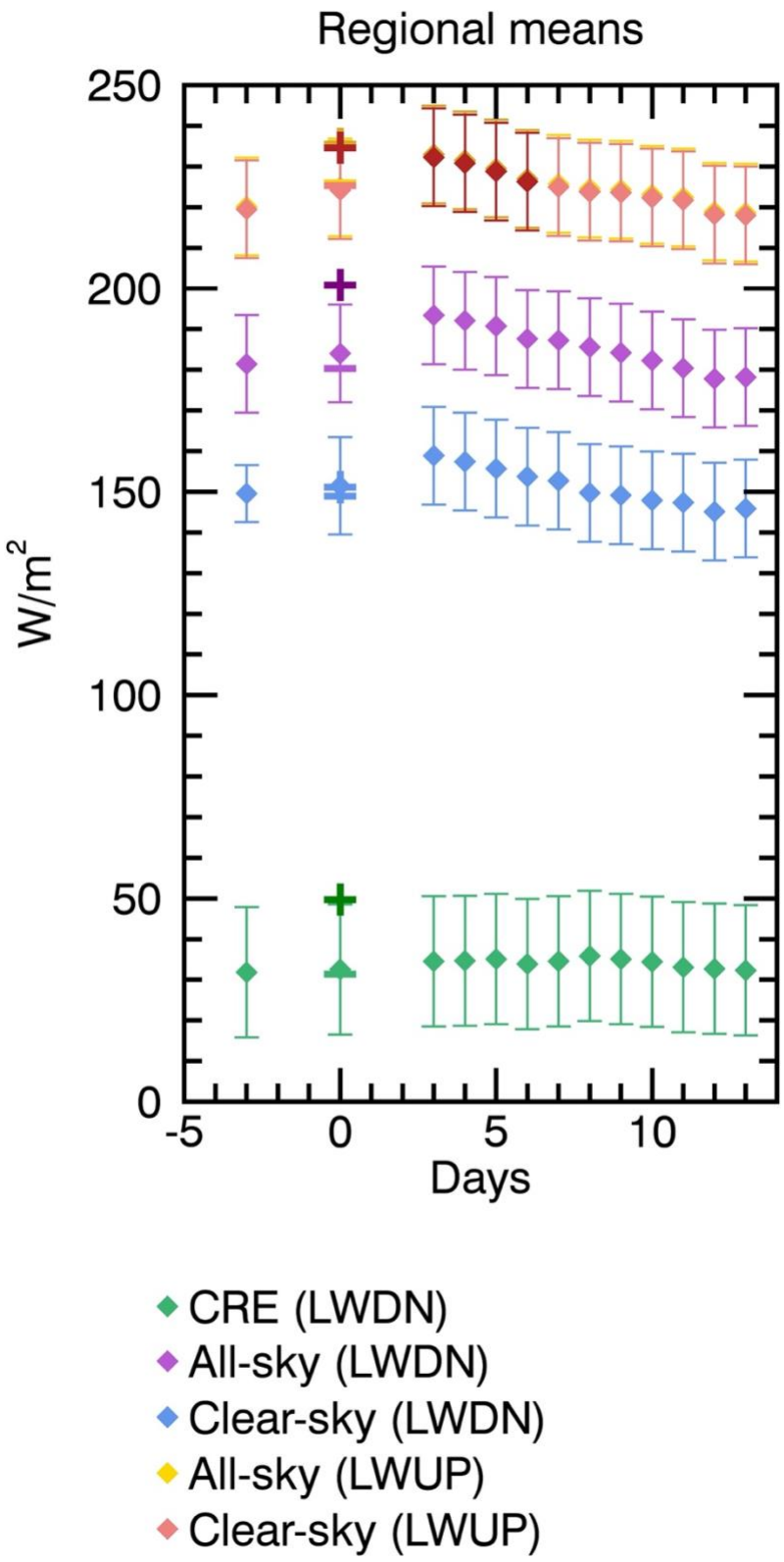
Regional means
250
200
150
100
50
0
W/m2
-5
0
5
10
Days
CRE (LWDN)
All-sky (LWDN)
Clear-sky (LWDN)
All-sky (LWUP)
Clear-sky (LWUP)

503

Figure 6. Regionally-averaged, 5-day running mean time series of surface all-sky and clear-sky, upwelling and downwelling LW (LWUP and LWDN, respectively) radiation and LW CRE across a polynya event. Error bars (mean ± combined uncertainty) represent the ±1σ uncertainty, and identify levels where σ confidence is reached. The average values over filtered polynya points (SIC <60%) are indicated with a "+" and ice points (SIC ≥ 85%) with a "-". Day 0 represents average value across all events; negative (positive) days are days leading up to (following) an event. Darkened points represent timestamps when the differences between the point in question and data collected "before" are statistically significant with $p < 0.05$ as determined by a Students-t difference of means test.

3.5 Influence of turbulent surface fluxes on cloud property vertical profiles

The leading hypothesis of the cloud response to a polynya opening is that increased surface turbulent fluxes warm and moisten the lower atmosphere facilitating cloud development (e.g. Smith et al., 1983). A recent study on the relationship between cloud cover and sea ice lead presence indicates that the increased LH fluxes promote increased cloud cover, whereas increased SH decreased cloud cover (Li et al., 2020a, 2020b). This is an important distinction that we evaluate using polynya events.

Figure 7 illustrates strong positive correlations between the surface turbulent fluxes as obtained from MERRA-2 and ERA5 and AIRS-based over the polynya but weak correlations over ice. Considering the agreement in SIC between the data sets, the better agreement in surface turbulent fluxes over the polynya suggest that SIC is the dominant control. Over ice-covered regions, where SIC is a weak control of surface turbulent fluxes, large SH and LH flux discrepancies suggest that differences in the input parameters, representations for surface

conditions, and the parameterizations for very stable boundary layers force this disagreement. While lowering confidence, the differences in the absolute value of the surface turbulent fluxes do not preclude any data set from tracking the relative changes; however, it is important to highlight the unrealistic SH (>100 W m^{-2}) and LH (>40 W m^{-2}) fluxes over sea ice often found by MERRA-2.

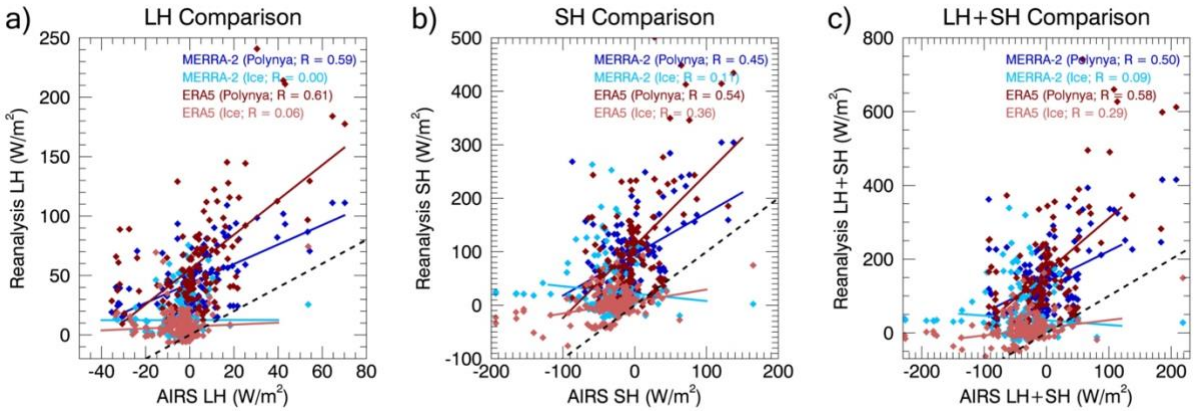

Figure 7. Scatterplot of the relationships between (a) LH, (b) SH, and (c) LH+SH from the AIRS-based, MERRA-2, and ERA5 data sets stratified by surface type: over polynya (darker hues) and ice (lighter hues) footprints. Black dashed line represents the one-to-one line and solid lines show linear regressions between each reanalysis and the AIRS-based data set.

Figures 8 and 9 show linear regression slopes between CF and LWC profiles and LH, SH, and combined LH + SH from the AIRS-based, MERRA-2, and ERA5 data sets during a polynya event. For polynya footprints, near-surface (below 1.5 km) CF shows the largest sensitivity to increased LH and SH fluxes, decreasing with altitude. The magnitudes of the maxima from each data set are very similar, ~0.004-0.006 in CF per 1 W m^{-2} increase in LH flux; the largest disagreement is in the heights where these maxima occur. Considering LWC regression slopes, results indicate similar behavior over polynya footprints with a switch in sign (AIRS-based, MERRA-2) or an

approach to zero (ERA5) occurring near 800 m; below this level enhanced surface fluxes lead to greater LWC (up to ~0.0003 g m^{-3} per W m^{-2}) and above this level no change (ERA5) or less LWC (AIRS-based, MERRA-2; up to -0.0003 g m^{-3} per W m^{-2}; Fig. 9).

The results indicate a different sensitivity of the CF and LWC profiles to LH versus SH. The CF increase due to LH over polynya footprints is almost double that of SH or the combined LH + SH, suggesting that LH fluxes have a larger effect on cloud cover over the polynya than SH. This result is consistent with the suggestion by Li et al. (2020b) of different sensitivities of the cloud response to LH and SH flux perturbations. The regression slope between CF and AIRS-based surface turbulent fluxes peaks near 200-300 m, approaches zero near 1.3 to 1.7 km, and then becomes slightly negative; according to MERRA-2 and ERA5, the largest enhancements to cloud cover occur at a slightly higher altitude from 500 m to 1.4 km before approaching zero. Overall, MERRA-2 and ERA5 exhibit similar regression slope profiles over polynya footprints (Fig. 8).

The three sources of surface turbulent fluxes result in differing cloud property sensitivity profiles over ice footprints (Figs. 8 and 9). AIRS-based fluxes suggest that the near-surface CF and LWC responses over ice indicate a reduction in CF and LWC with increased surface turbulent fluxes below ~700 m (largest reduction near 300 m) but a pronounced layer of increased cloud cover and LWC immediately above. The increased LWC over ice footprints near 1.0 km is captured in ERA5 (Fig. 9, bottom row), but not MERRA-2 (Fig. 9, middle row). Enhanced LH drives the largest changes in cloud cover over ice, with reductions of up to 0.011 in CF and ~0.015 g m^{-3} per W m^{-2} in LWC near 400 m and increases of up to 0.007 in CF and 0.008 g m^{-3} in LWC near 1 km; these effects are four times larger than that due to SH or the combined LH + SH (Figs. 8 and 9, top row). MERRA-2 fluxes also indicate a reduction in CF over ice between 300 m and 1.3 km in response to increased LH, SH, and LH+SH fluxes, similar to the AIRS-based data.

Different from the AIRS-based data set, there is no cloud response outside of the 300 m to 1.3 km altitude range, and magnitudes are much smaller (Fig 8, middle row). ERA5 disagrees with both AIRS-based and MERRA-2, suggesting an increase in cloud cover nearly double that over polynya footprints (Fig. 8, bottom row). Additionally, over ice footprints, CF profile regression slopes using AIRS-based LH, SH, and LH+SH fluxes suggest an upward shift in CF, a relative increase aloft that is captured by ERA5 (in addition to increases at the surface) but not evident with MERRA-2 (Fig. 8). As with regression slopes over polynya footprints, changes to LH seem to drive significantly larger responses in comparison to changes to SH or the combined LH+SH. Accounting for ranges of uncertainty, LWC over ice is near zero below 3 km using MERRA-2 fluxes, suggesting little coupling between surface turbulent heat fluxes and cloud properties over ice footprints (Fig. 9, middle row). Similar to CF, the largest impacts across AIRS-based and MERRA-2 data sources in LWC are observed when additional LH is added; increases over the polynya are up to double that of SH over the polynya and for ice over triple that of SH (Figs. 8 and 9, top and middle rows). However, for ERA5 the LWC response to LH over ice footprints is of opposite sign to that of SH and LH+SH and regression profiles between LWC and SH and combined LH + SH largely agree with those observed by the AIRS-based, albeit with smaller near-surface magnitudes for the latter (Fig. 9, bottom row). A similar analysis was completed for IWC but is not shown due to low confidence.

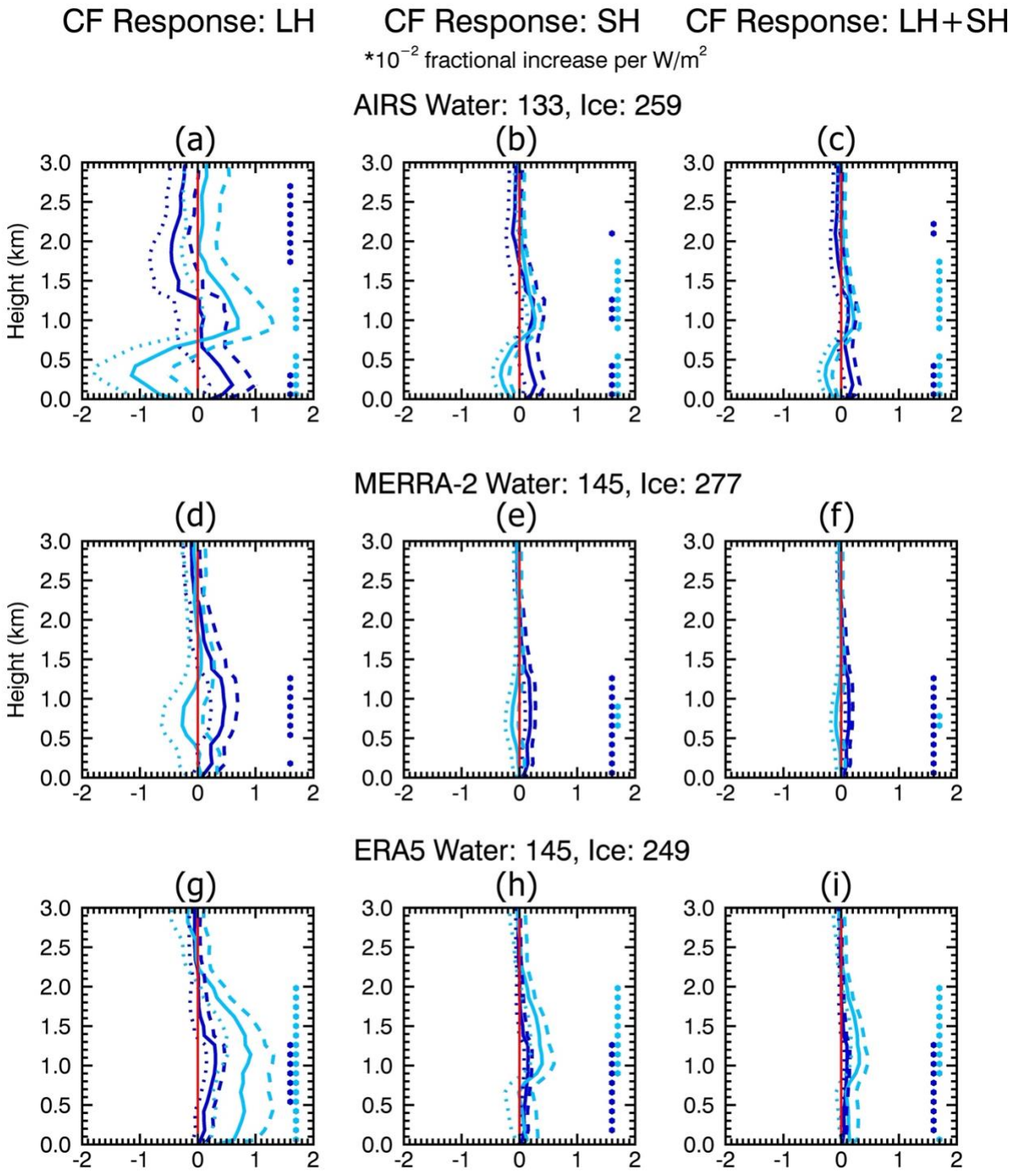

Figure 8. Sensitivity of CF 0-3km vertical profile for filtered ice (SIC ≥ 85%, cyan) and polynya (SIC <60%, blue) footprints to changes in (a,d) surface LH, (b,e) SH and (c,f) LH + SH using the AIRS-based (a-c), MERRA-2 (d-f), and ERA5 (g-i) surface turbulent flux data sets. Hashed lines

590 (mean + 2σ uncertainty) and dotted lines (mean – 2σ uncertainty) identify the 95% confidence
591 interval. Vertical dark blue (light blue) dots on the right side of each panel represent levels where
592 the regression slope is statistically significantly distinguishable from zero (positive or negative).
593

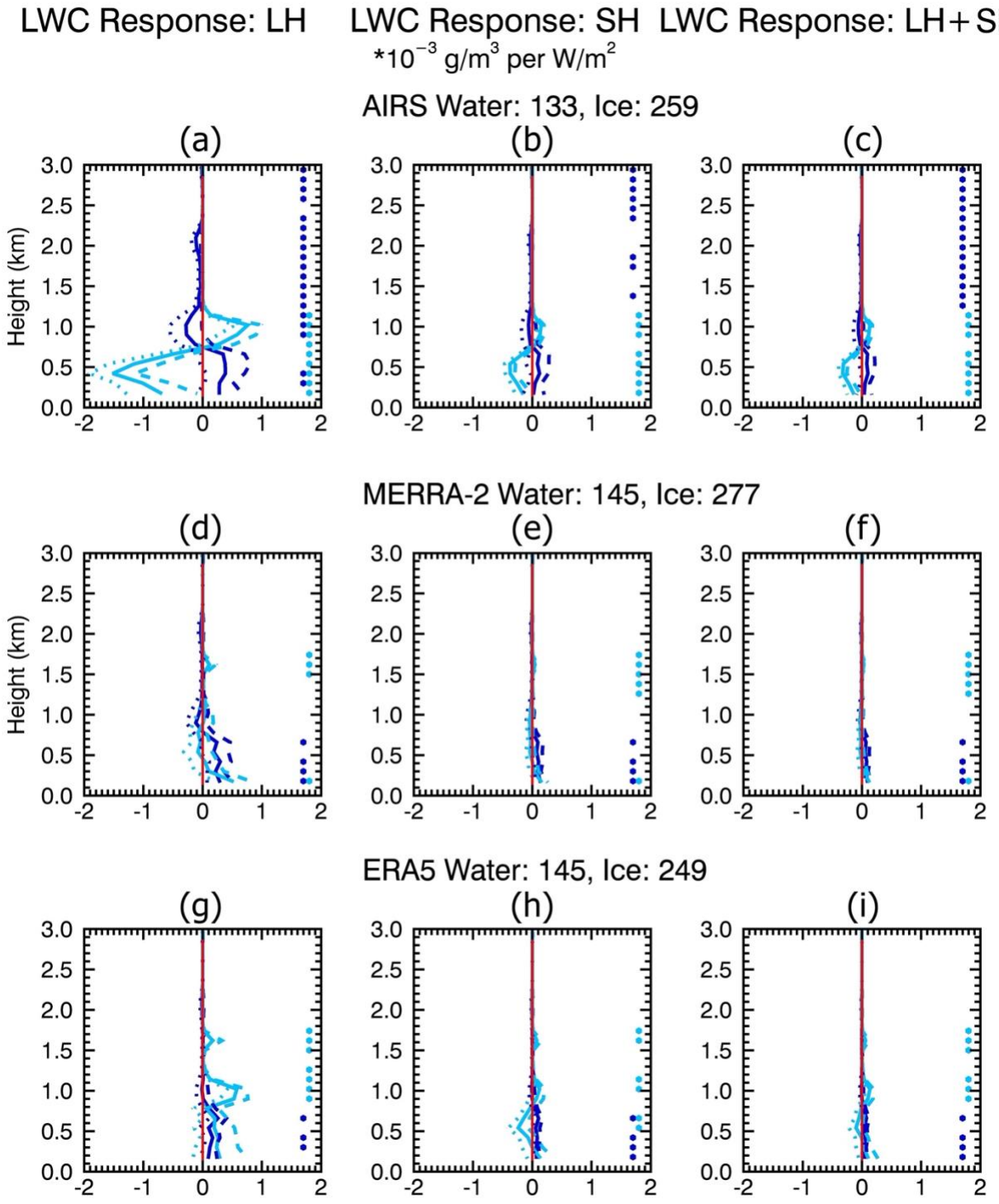

Figure 9. Sensitivity of LWC 0-3 km vertical profiles over filtered ice (SIC ≥ 85%, cyan) and polynya (SIC <60%, blue) footprints to changes in (a,d) LH, (b,e) SH, and (c,f) LH + SH using the AIRS-based (a-c), MERRA-2 (d-f), and ERA5 (g-i) surface turbulent fluxes. Hashed lines (mean

598 + 2σ uncertainty) and dotted lines (mean – 2σ uncertainty) identify the 95% confidence interval.
599 Vertical dark blue (light blue) dots on the right side of each panel represent levels where the
600 regression slope is statistically significantly distinguishable from zero (positive or negative).
601
602 Figure 10 shows the same regression approach, but replacing LH and SH fluxes with SIC.
603 Surface turbulent fluxes are expected to scale with SIC. The results in Fig. 8 show consistency
604 with the CF and LWC regression slope profiles computed with the surface turbulent fluxes data.
605 Despite the low confidence in the surface turbulent flux data sets, the results using SIC, a higher
606 confidence measurement, are consistent. This lends confidence to the general nature of our results,
607 however the quantitative sensitivities shown contain substantial uncertainty. Additionally, the
608 larger noise (and subsequent uncertainty) in regression slopes below 1 km likely results from the
609 surface-atmosphere interactions themselves. We do not take the statistical significance shown at
610 higher altitudes (>2.5 km) as an indication of a response to the surface perturbation.

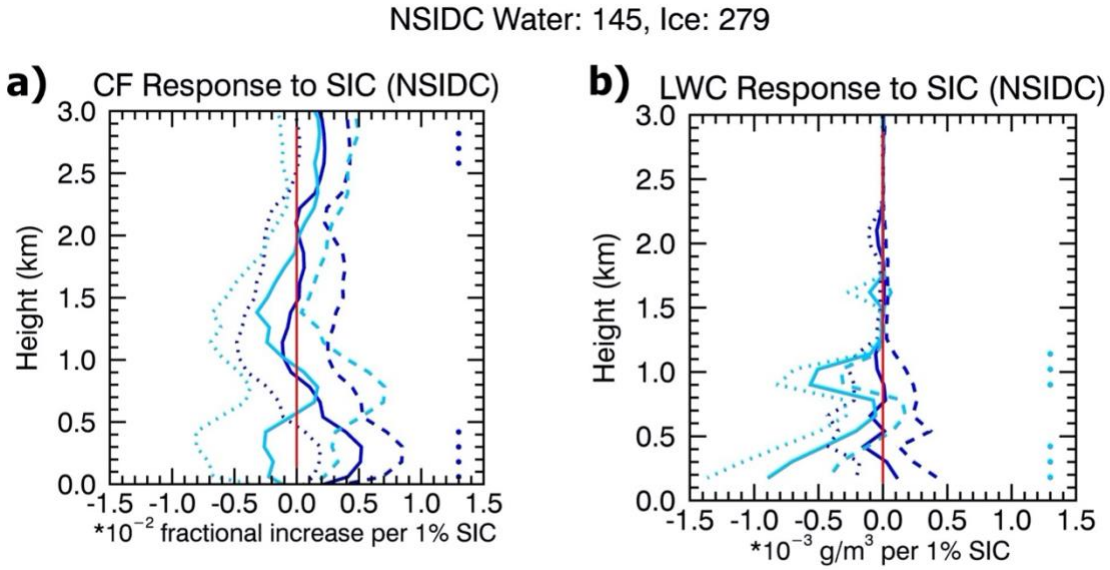

611
612 **Figure 10**. Sensitivity of the (a) CF and (b) LWC 0-3 km vertical profiles over filtered ice (SIC ≥
613 85%, light blue) and polynya (SIC <60%, dark blue) footprints to changes in sea ice concentration

(SIC). Hashed lines (mean + 2σ uncertainty) and dotted lines (mean – 2σ uncertainty) identify the 95% confidence interval. Vertical dark blue (light blue) dots on the right side of each panel represent levels where the regression slope is statistically significantly distinguishable from zero (positive or negative).

4 Discussion

We present a satellite-based analysis of the response and radiative impact of clouds to the NoW polynya. Our approach exploits the periodic opening of the NoW polynya and the near-step change in sea ice cover as a natural laboratory to quantify the cloud response to a changing sea ice cover. The advantage of our approach is that we can define an experimental control (ice surface type) subject to the same large-scale meteorological conditions as the areas affected by the sea ice perturbation (polynya surface type). Thus, the quantified cloud response to the sea ice perturbation does not rely on meteorological reanalysis. Limitations of this study include the small sample size and the possibility that in focusing on shallow clouds and low-level effects of surface cover change, the study is slightly affected by beam attenuation in cloudy environments (Blanchard et al., 2014; Liu et al., 2017). An additional caveat is the potential influence of polynya-scale circulations that could influence the comparison; however, given the large number of different polynya sizes and durations averaged over, this feature is not expected to have a significant effect. Our approach is unique and compliments previous investigations of Arctic cloud-sea ice interactions relying on internal variability. Overall, we find results similar to such previous studies.

The occurrence of the NoW polynya uncovers warmer ocean water to the colder winter atmosphere driving a surface skin and near-surface air temperature gradient that causes upward SH and LH fluxes. Differences in SH and LH fluxes between the MERRA-2, ERA5, and AIRS-

based data sets are underscored by differences in input parameterization schemes, sea ice characterization and representation, and environmental temperature and humidity. The poor representation of sea ice and snow cover on sea ice likely causes a warm bias in the skin temperatures in MERRA-2 and ERA5 (Batrak & Müller, 2019) and the thermal stratification of the lower atmosphere, and could explain why reanalysis SH and LH fluxes are always positive and much larger than satellite-retrieved. AIRS-based skin temperature is produced from retrievals of surface emissivity and is likely more accurate (Susskind et al., 2013). Another factor effecting greater differences between the three data sets could be the poor representation of boundary layer stability and thermal structure over the sea ice in the parameterization of the fluxes by MERRA-2 and ERA5 compared to the AIRS-derived fluxes.

In response to this substantial surface-to-atmosphere energy and moisture transfer, the cloud cover and condensate amounts are hypothesized to increase (e.g., Gultepe et al., 2003). Our results demonstrate statistically significant increases in CF and LWC in the near-surface (0-3 km) layer over the polynya, as well as across the NoW region. Similarly, Weijer et al. (2017) found enhanced surface turbulent fluxes and changes to cloud properties associated with polynya occurrence in a modeling analysis of Antarctic polynyas. Comparing profiles over polynyas with those over nearby ice, CF is larger over the polynya than nearby ice (by as much as 30%). The LWC profile was similarly affected by the removal of sea ice cover, increasing by greater than 50% and up to 350%. The magnitude of the CF changes from previous work on the cloud response to sea ice declines using interannual variability is 5-10% (Kay & Gettelman, 2009; Morrison et al., 2018; Palm et al., 2010; Taylor et al., 2015; Wu & Lee, 2012), a smaller response than in the context of the NoW polynya. This larger CF response to sea ice loss in the context of the polynya is expected as the surface turbulent flux forcing is substantially stronger and because the influence of sea ice cover

change on clouds is isolated in our approach. Alternatively, the altitude ranges of greatest change in CF and LWC are consistent with previous studies (e.g., Kay & Gettelman, 2009; Morrison et al., 2018; Taylor et al., 2015). This suggests that some aspects of the boundary layer processes and cloud response to the sea ice perturbation from the polynya may be generalizable to the Arctic-wide cloud response to sea ice decline; however, more data is needed to explore this potential generalizability. Aerosols sourced by the polynya could be a confounding variable influencing cloud development (e.g. Creamean et al., 2020; Tobo et al., 2019; Yan et al. 2020); however, data is not available for such an analysis. Our results support the hypothesis that polynyas create conditions more favorable for cloud development through increased surface turbulent fluxes that warm and moisten the overlying atmosphere.

Further delving into cloud composition over the polynya, clouds are dominated by more liquid particles closer to the surface (below approximately 500 m) and more ice particles aloft (above 500 m). Results from Morrison et al. (2018) indicate a similar cloud structure, with a greater liquid cloud fraction reported over the polynya, especially in the lowest 2 km. Over ice footprints, ice particles dominate the entire 0-3 km layer, though liquid particles are more common closer to the surface; this is in agreement with Morrison et al. (2018) where the greatest liquid cloud fraction was observed closest to the surface with a monotonic decrease with height. Though our results do not show a monotonic decrease with height, the spatial and temporal domains of the studies are different. Over polynya footprints, liquid particles are dominant near the surface (below 500 m) and concentrations quickly decrease with height above this level and ice particles then dominate.

The cloud response to the polynya event does not abruptly stop upon closing. Though the regional SIC rises back above the 85% threshold, small pockets of open water remain, and ice growth and lingering warm, moist air and clouds continue to affect the surface energy budget. We

683 find a lingering cloud property and radiative fluxes as well as temperature and humidity effects
684 (Fig. S4) in agreement with Boisvert et al. (2012), that is also influenced by changing meteorology
685 (Figs. S1-S3). Specifically, we find an enhancement in regional low-cloud cover in the days
686 following polynya closure relative to that observed prior to the polynya opening, in part due to the
687 lack of processes removing the excess energy, moisture, and cloud condensate from the region
688 (e.g. Herman & Goody, 1976) and in part due to a shift to southerly large-scale wind flow.

689 Lastly, our results point to a cloud effect on polynya lifetime. During the polynya event, our
690 results show that the LW CRE is 18 W m^{-2} larger over water than ice footprints. Though cloud
691 amount in the period following the event is greater than that observed before the event, this trend
692 is not upheld by LW CRE results when comparing the before and after periods or when analyzing
693 stepped means in the two weeks following the polynya. We speculate that downwelling longwave
694 impacts from enhanced cloud cover after the polynya are likely balanced by the gradual spread of
695 warmer and moister air created by the polynya and the shift to southerly winds increasing the clear
696 sky LW flux.

697 **5 Summary and Conclusion**

698 This paper offers an in-depth analysis of the cloud and surface energy budget response to a
699 near-step change in sea ice cover created by the North Water Polynya. This study pairs active
700 remotely sensed satellite data from the NASA C3M merged product with collocated MERRA-2,
701 ERA5, and AIRS-based derived surface turbulent fluxes. The relationship between surface cover
702 and the overlying cloud and radiative response is determined by sorting each footprint by SIC then
703 aggregating corresponding atmospheric data accordingly.

704 A statistically significant and pronounced increase in low-cloud amount over polynya
705 footprints is observed during a composite polynya event, with up to 200% more clouds over the

polynya in comparison to that over nearby ice. Strong variation occurs on a track-to-track basis, but results confirm that differences in cloud property profiles over polynya versus those over nearby ice are non-zero and favor more clouds over the polynya. The largest differences are observed between 700 m and 1.2 km, coinciding with the LoM CF over both ice and polynya surface classifications. Within this altitude range, LWC is largest over polynya footprints, with the LWC maximum altitude over ice observed closer to the surface. Despite larger uncertainty associated with IWC, averaged profiles show similar results, with a broad maximum occurring in a layer from ~700 m to 1.3 km.

Upwelling and downwelling LW radiation, the LW CRE, and cloud cover peak during the event; however, the "closure" of the polynya does not indicate a return to pre-event conditions. Instead, regionally averaged surface temperatures after the event more closely match those observed over the polynya during the event, cloud cover remains elevated, and LW radiation (upwelling and downwelling) remains elevated in the days following the polynya, only approaching pre-polynya levels between 5 and 7 days following the closure.

Increased surface turbulent LH and SH fluxes are associated with increased CF over the polynya and decreased CF over ice in the layer closest to the surface, though the altitude of the largest impacts varies based on the surface turbulent flux data set. AIRS-based results suggest the impact to LWC generally mirrors that of CF, but those from MERRA-2 and ERA5 paint a different picture. The largest impacts on CF and LWC are attributed to changes in LH when compared to that from SH or the combined LH + SH. Differences in the three data sets represent a significant limitation of this and related analyses. Improved surface turbulent data sets are critical to advancing our understanding of the cloud response to sea ice decline.

728 This small-scale regional analysis highlights the dependence of low-cloud and the local surface
729 energy budget on changes in surface sea ice cover and the releases of heat and moisture from the
730 ocean surface, associated with the opening of a polynya. These results suggest that a widespread
731 reduction in sea ice can cause increases in overlying cloud cover, leading to a positive feedback
732 where substantial and localized radiative effects slow the refreezing. However, increases in active
733 sensor coverage and a greater amount of *in situ* surface turbulent flux data are needed to further
734 refine the results discussed in this study. Additionally, these conclusions highlight the need for a
735 better understanding of feedbacks that potentially expand the length of polynyas, and underscore
736 the uncertainties involved in developing forecasts for the Arctic in a warming world.
737
738 **Acknowledgments**
739 The work of E. Monroe and P. Taylor was funded in part by the NASA Interdisciplinary Studies
740 Program grant NNH12ZDA001N-IDS and the NASA Radiation Budget Science Project. The
741 work of L. Boisvert was funded by the NASA GSFC Cryospheric Sciences ISFM work package.
742 The C3M data used in this analysis is available from the NASA Langley Atmospheric Science
743 Data Center (https://asdc.larc.nasa.gov). The MERRA-2 data is available from the NASA
744 Goddard Earth Sciences Data and Information Services Center (https://disc.gsfc.nasa.gov). The
745 AIRS-based surface turbulent flux data is available from the NASA GSFC Cryospheric Sciences
746 Laboratory (https://earth.gsfc.nasa.gov/cryo/data/airs-derived-turbulent-fluxes-northwater-
747 polynya).
748
749
750 **6 References**
751

752 April, A., Montpetit, B., & Langlois, D. (2019). Linking the open water area of the North Open
753 Water Polynya to climatic parameters using a multiple linear regression prediction model.
754 *Atmosphere-Ocean*, 57(2), 91-100. https://doi.org/10.1080/07055900.2019.1598332
755
756 Alkama, R., Cescatti, A., Taylor, P. C., Garcia-San Martin, L., Douville, H., Duveiller, G., et al.
757 (2020). Clouds damp the radiative impacts of polar sea ice loss. *The Cryosphere*, 14, 2673-2686.
758 https://doi.org/10.5194/tc-14-2673-2020
759
760 Andreas, E. L., Horst, T. W., Grachev, A. A., Persson, P. O. G., Fairall, C. W., Guest, P. S.,
761 & Jordan, R. E. (2010a). Parametrizing turbulent exchange over summer sea ice and the marginal
762 ice zone. *Quarterly Journal of the Royal Meteorological*
763 *Society*, 136(649), 927– 943. https://doi.org/10.1002/qj.618
764
765 Andreas, E. L., Persson, P. O. G., Grachev, A. A., Jordan, R. E., Horst, T. W., Guest, P. S.,
766 & Fairall, C. W. (2010). Parameterizing turbulent exchange over sea ice in winter. *Journal of*
767 *Hydrometeorology*, 11(1), 87– 104. https://doi.org/10.1175/2009JHM1102.1
768
769 Avery, M., Winker, D., Heymsfield, A., Vaughan, M., Young, S., Hu, Y., & Trepte,
770 C. (2012). Cloud ice water content retrieved from the CALIOP space-based lidar. *Geophysical*
771 *Research Letters*, 39, L05808. https://doi.org/10.1029/2011GL050545
772

Barber, D. G., Hanesiak, J. M., Chan, J., & Piwowar, J. (2001), Sea-ice and meteorological conditions in northern Baffin Bay and the North Water polynya between 1979 and 1996. *Atmosphere-Ocean*, 39, 343–359. https://doi.org/10.1080/07055900.2001.9649685.

Barton, N. P., Klein, S. A., Boyle, J. S., & Zhang, Y. Y. (2012). Arctic synoptic regimes: Comparing domain-wide Arctic cloud observations with CAM4 and CAM5 during similar dynamics. *Journal of Geophysical Research*, 117, D15205. https://doi.org/10.1029/2012JD017589

Batrak, Y. & Müller, M. (2019). On the warm bias in atmospheric reanalyses induced by the missing snow over Arctic sea-ice. *Nature Communications*, 10(1), 4170. https://doi.org/10.1038/s41467-019-11975-3

Blanchard, Y., Pelon, J., Eloranta, E. W., Moran, K. P., Delanoë, J., & Sèze, G. (2014). A synergistic analysis of cloud cover and vertical distribution from A-Train and ground-based sensors over the high Arctic station Eureka from 2006 to 2010. *Journal of Applied Meteorology and Climatology*, 53(11), 2553-2570. https://doi.org/10.1175/JAMC-D-14-0021.1

Boisvert, L. N., Markus, T., Parkinson, C. L., & Vihma, T. (2012). Moisture fluxes derived from EOS Aqua satellite data for the North Water polynya over 2003-2009. *Journal of Geophysical Research*, 117, D06119. https://doi.org/10.1029/2011JD016949

795 Boisvert, L., Vihma, T., & Shie, C. L. (2020). Evaporation from the Southern Ocean estimated
796 on the basis of AIRS satellite data. *Journal of Geophysical Research: Atmospheres*, *125*(1),
797 e2019JD030845. https://doi.org/10.1029/2019JD030845
798
799 Boisvert, L. N., Wu, D. L., & Shie, C. L. (2015). Increasing evaporation amounts seen in the
800 Arctic between 2003 and 2013 from AIRS data. *Journal of Geophysical Research:*
801 *Atmospheres*, *120*(14), 6865-6881. https://doi.org/10.1002/2015JD023258
802
803 Bosilovich, M. G., Akella, S., Coy, L., Cullather, R., Draper, C., Gelaro, R., et al. (2016).
804 MERRA-2. Initial evaluation of the climate, in *Global Modeling and Data Assimilation*,
805 Technical Report Series, vol. 43, edited by R. D. Koster NASA/TM-2015-104606, 139 pp.,
806 Goddard Space Flight Center, Greenbelt, Md.
807
808 Burt, M. A., Randall, D. A., & Branson, M. D. (2016). Dark Warming. *Journal of Climate*, 29(2),
809 705-719. https://doi.org/10.1175/JCLI-D-15-0147.1
810
811 Cavalieri, D. J., Parkinson, C. L., Gloersen, P., & Zwally, H. J. (1996, updated yearly). *Sea Ice*
812 *Concentrations from Nimbus-7 SMMR and DMSP SSM/I-SSMIS Passive Microwave Data,*
813 *Version 1*. [NSIDC-0051]. Boulder, Colorado USA. NASA National Snow and Ice Data Center
814 Distributed Active Archive Center. https://doi.org/10.5067/8GQ8LZQVL0VL
815

816 Cohen, J., Screen, J. A., Furtado, J. C., Barlow, M., Whittleston, D., Coumou, D., et al. (2014).
817 Recent Arctic amplification and extreme mid-latitude weather. *Nature Geoscience*, 7, 627-637.
818 https://doi.org/10.1038/ngeo2234
819
820 Creamean, J. M., Hill, T. C. J., DeMott, P. J., Uetake, J., Kreidenweis, S., & Douglas, T. A.
821 (2020). Thawing permafrost: an overlooked source of seeds for Arctic cloud formation.
822 *Environmental Research Letters*, 15, 084022. https://doi.org/10.1088/1748-9326/ab87d3
823
824 Cullather, R., Hamill, T. M., Bromwich, D., Wu, X., & Taylor, P. C. (2016). Systematic
825 Improvements of Reanalyses in the Arctic (SIRTA): A White Paper. Inter-agency Arctic
826 Research Policy Committee (IARPC) Principals. https://www.iarpccollaborations.org/news/6004
827
828 Curry, J. A., Schramm, J. L., Rossow, W. B., & Randall, D. (1996). Overview of Arctic cloud
829 and radiation characteristics. *Journal of Climate*, 9(8), 1731-1764. https://doi.org/10.1175/1520-
830 0442(1996)009<1731:OOACAR>2.0.CO;2
831
832 Donlon, C. J., Martin, M., Stark, J., Roberts-Jones, J., Fiedler, E., & Wimmer, W. (2012). The
833 Operational Sea Surface Temperature and Sea Ice Analysis (OSTIA) system. *Remote Sensing of*
834 *the Environment*, 116, 140–158. https://doi.org/10.1016/j.rse.2010.10.017
835
836 Dunbar, M. & Dunbar, M. J. (1972). The history of the North Water. *Proceedings of the Royal*
837 *Society of Edinburgh, Section B: Biological Sciences*, 72(1), 231-241.
838 https://doi.org/10.1017/S0080455X00001788

Eastwood, S., Lavergne, T., & Tonboe, R. (2014). Algorithm theoretical basis document for the OSI SAF global reprocessed sea ice concentration product. *EUMETSAT Network Satellite Application Facilities.*

Gelaro, R., McCarty, W., Suárez, M. J., Todling, R., Molod, A., Takacs, L., et al. (2017). The Modern-Era Retrospective Analysis for Research and Applications, version-2 (MERRA-2). *Journal of Climate*, 30, 5419-5454. https://doi.org/10.1175/JCLI-D-16-0758.1

Grachev, A. A., Andreas, E. L., Fairall, C. W., Guest, P. S., & Persson, P. O. G. (2007). SHEBA flux–profile relationships in the stable atmospheric boundary layer. *Boundary-Layer Meteorology*, 124(3), 315– 333. https://doi.org/10.1007/s10546-007-9177-6

Gultepe, I., Isaac, G. A., Williams, A., Marcotte, D., & Strawbridge, K. B. (2003). Turbulent heat fluxes over leads and polynyas, and their effects on Arctic clouds during FIRE.ACE: Aircraft observations for April 1998. *Atmosphere-Ocean*, 41(1), 15– 34. https://doi.org/10.3137/ao.410102

Hegyi, B. M., & Taylor, P. C. (2017). The regional influence of the Arctic Oscillation and Arctic Dipole on the wintertime Arctic surface radiation budget and sea ice growth. *Geophysical Research Letters*, 44(9), 4341-4350. https://doi.org/10.1002/2017GL073281

Helfand, H. M., & Schubert, S. D. (1995). Climatology of the simulated Great Plains low-level jet and its contribution to the continental moisture budget of the United States. *Journal of Climate*, **8**, 784–806. https://doi.org/10.1175/1520-0442(1995)008<0784:COTSGP>2.0.CO;2

Henderson, D. S., L'Ecuyer, T., Stephens, G., Partain, P., & Sekiguchi, M. (2013). A multisensor perspective on the radiative impacts of clouds and aerosols, *Journal of Applied Meteorology and Climatology*, 52(4), 853-871. https://doi.org/10.1175/JAMC-D-12-025.1

Herman, G., & Goody, R. (1976). Formation and persistence of summertime Arctic stratus clouds. *Journal of Atmospheric Science*, 33(8), 1537-1553. https://doi.org/10.1175/1520-0469(1976)033<1537:FAPOSA>2.0.CO;2

Hersbach, H., Bell, B., Berrisford, P., Biavati, G., Horányi, A., Muñoz Sabater, J., et al. (2018). ERA5 hourly data on single levels from 1979 to present. Copernicus Climate Change Service (C3S) Climate Data Store (CDS). (Accessed on 18-03-2021). https://doi.org/10.24381/cds.adbb2d47

Hersbach, H., Bell, B., Berrisford, P., Hirahara, S., Horányi, A., Muñoz Sabater, J., et al. (2020). The ERA5 global reanalysis. *Quarterly Journal of the Royal Meteorological Society*, 146, 1999-2049. https:///doi.org/10.1002/qj.3803

Holtslag, A. A. M., & de Bruin, H. A. R. (1988). Applied modeling of the nighttime surface energy balance over land. *Journal of Applied Meteorology*, 27(6), 689-704. https://doi.org/10.1175/1520-0450(1988)027<0689:AMOTNS>2.0.CO;2

IFS Documentation–Cy41r2 (2016), Operational implementation 8 March 2016, Part IV: Physical processes, ECMWF, Reading, U. K.

Ito, H. (1982). Sea-ice atlas of northern Baffin Bay. Special Issue of Zuricher Geographische Schriften, No. 7 (ZGS 7), Zurich, 142 pp.

Kato, S., Sun-Mack, S., Miller, W. F., Rose, F. G., Chen, Y., Minnis, P., & Wielicki, B. A. (2010). Relationships among cloud occurrence frequency, overlap, and effective thickness derived from CALIPSO and CloudSat merged cloud vertical profiles, *Journal of Geophysical Research*, 115, D00H28, doi:10.1029/2009JD012277.

Kato, S., Rose, F. G., Sun-Mack, S., Miller, W. F., Chen, Y., Rutan, D. A., et al. (2011). Improvements of top-of-atmosphere and surface irradiance computations with CALIPSO-, CloudSat-, and MODIS-derived cloud and aerosol properties. *Journal of Geophysical Research*, 116, D19209. https://doi.org/10.1029/2011JD016050

Kay, J. E., & Gettelman, A. (2009). Cloud influence on and response to seasonal Arctic sea ice loss. *Journal of Geophysical Research*, 114, D18204. https://doi.org/10.1029/2009JD011773

Kottmeier, C., & Engelbart, D. (1992). Generation and atmospheric heat exchange of coastal polynyas in the Weddell Sea. *Boundary-Layer Meteorology*, 60(3), 207– 234. https://doi.org/10.1007/BF00119376

Kwok, R., Kurtz, N. T., Brucker, L., Ivanoff, A., Newman, T., Farrel, S. L., et al. (2017). Intercomparison of snow depth retrievals over Arctic sea ice from radar data acquired by Operation IceBridge. *The Cryosphere*, 11, 2571-2593. https://doi.org/10.5194/tc-11-2571-2017

Launiainen, J., & Vihma, T. (1990). Derivation of turbulent surface fluxes—An iterative flux-profile method allowing arbitrary observing heights. *Environmental Software*, 5(3), 113– 124. https://doi.org/10.1016/0266-9838(90)90021-W

Li, X., Krueger, S. K., Strong, C., & Mace, G. G. (2020a). Relationship between wintertime leads and low clouds in the pan-Arctic. *Journal of Geophysical Research: Atmospheres*, 125, e2020JD032595. https://doi.org/10.1029/2020JD032595

Li, X., Krueger, S. K., Strong, C., Mace, G. G., & Benson, S. (2020b). Midwinter Arctic leads form and dissipate low clouds. *Nature Communications*, 11, 206. https://doi.org/10.1038/s41467-019-14074-5

Lindsay, R., Wensnahan, M., Schweiger, A., & Zhang, J. (2014). Evaluation of seven different atmospheric reanalysis products in the Arctic. *Journal of Climate*, 27(7), 2588– 2606. https://doi.org/10.1175/JCLI-D-13-00014.1

928

929 Liu, Y., Shupe, M. D., Wang, Z., & Mace, G. (2017). Cloud vertical distribution from combined
930 surface and space radar-lidar observations at two Arctic atmospheric observatories. *Atmospheric*
931 *Chemistry and Physics*, 17, 5973-5989. https://doi.org/10.5194/acp-17-5973-2017

932

933 Melling, H., Gratton, Y., & Ingram, G. (2001). Ocean circulation within the North Water
934 polynya of Baffin Bay. *Atmosphere-Ocean*, 39(3), 301-325.
935 https://doi.org/10.1080/07055900.2001.9649683

936

937 Morales Maqueda, M. A., Willmott, A. J., & Biggs, N. R. T. (2004). Polynya dynamics: a review
938 of observations and modeling. *Reviews of Geophysics*, 42(1).
939 https://doi.org/10.1029/2002RG000116

940

941 Miller, N. B., Shupe, M. D., Cox, C. J., Noone, D., Persson, P. O. G., & Steffen, K. (2017).
942 Surface energy budget responses to radiative forcing at Summit, Greenland. *The Cryosphere*, 11,
943 497–516. https://doi.org/10.5194/tc-11-497-2017

944

945 Minnis, P., Sun-Mack, S., Young, D. F., Heck, P. W., Garber, D. G., Chen, Y., et al. (2011a).
946 CERES Edition-2 cloud property retrievals using TRMM VIRS and Terra and Aqua MODIS
947 data: Part I: Algorithms. *IEEE Transactions on Geoscience and Remote Sensing*, 49(11), 4374-
948 4400. https://doi.org/10.1109/TGRS.2011.2144601

949

950 Minnis, P., Sun-Mack, S., Chen, Y., Khaiyer, M. M., Yi, Y., Ayers, J. A., et al. (2011b). CERES
951 Edition-2 cloud property retrievals using TRMM VIRS and Terra and Aqua MODIS data: Part
952 II: Examples of average results and comparisons with other data. *IEEE Transactions on*
953 *Geoscience and Remote Sensing*, 49(11), 4401-4430.
954 https://doi.org/10.1109/TGRS.2011.2144602
955
956 Molod, A., Takacs, L., Suarez, M., & Bacmeister, J. (2015). Development of the GEOS-5
957 atmospheric general circulation model. Evolution from MERRA to MERRA2, *Geoscientific*
958 *Model Development*, 8(5), 1339–1356, https://doi.org/10.5194/gmd-8-1339-2015
959
960 Morrison, A. L., Kay, J. E., Chepfer, H., Guzman, R., & Yettella, V. (2018). Isolating the liquid
961 cloud response to recent Arctic sea ice variability using spaceborne lidar observations. *Journal of*
962 *Geophysical Research: Atmospheres*, 123, 473– 490. https://doi.org/10.1002/2017JD027248
963
964 Mysak, L. A., & Huang, F. (1992). A latent- and sensible-heat polynya model for the North
965 Water. *Journal of Physical Oceanography*, 22(6), 596-608. https://doi.org/10.1175/1520-
966 0485(1992)022<0596:ALASHP>2.0.CO;2
967
968 Palm, S. P., Strey, S. T., Spinhirne, J., & Markus, T. (2010). Influence of Arctic sea ice extent on
969 polar cloud fraction and vertical structure and implications for regional climate. *Journal of*
970 *Geophysical Research: Atmospheres*, 115, D21209. https://doi.org/10.1029/2010JD013900
971

Parkinson, C. L., & DiGirolamo, N. E. (2016). New visualizations highlight new information on the contrasting Arctic and Antarctic sea-ice trends since the late 1970s. *Remote Sensing of Environment*, 183, 198-204. https://doi.org/10.1016/j.rse.2016.05.020

Renfrew, I. A., King, J. C., & Markus, T. (2002). Coastal polynyas in the southern Weddell Sea: variability of the surface energy budget. *Journal of Geophysical Research: Oceans*, 107(C6), 16-1–16-22. https://doi.org/10.1029/2000JC000720

Reynolds, R. W., Smith, T. M., Liu, C., Chelton, D. B., Casey, K. S., & Schlax, M. G. (2007). Daily high-resolution-blended analyses for Sea Surface Temperature, *Journal of Climate*, 20, 5473-5496, https://doi.org/10.1175/2007JCLI1824.1

Roberts, A., Allison, I., & Lytle, V. I. (2001). Sensible- and latent-heat-flux estimates over the Mertz Glacier polynya, East Antarctica, from in-flight measurements. *Annals of Glaciology*, 33, 377-384. https://doi.org/10.3189/172756401781818112

Screen, J. A., & Simmonds, I. (2010). The central role of diminishing sea ice in recent Arctic temperature amplification. *Nature*, 464(7293), 1334-1337. https://doi.org/10.1038/nature09051

Screen, J. A., Bracegirdle, T. J., & Simmonds, I. (2019). Polar climate change as manifest in atmospheric circulation. *Current Climate Change Reports*, 4, 383-395. https://doi.org/10.1007/s40641-018-0111-4

995 Serreze, M. C., Barrett, A. P., Stroeve, J. C., Kindig, D. M., & Holland, M.M. (2009). The
996 emergence of surface-based Arctic amplification. *The Cryosphere*, 3, 11–19.
997 https://doi.org/10.5194/tc-3-11-2009
998
999 Shupe, M. D., Persson, P. O. G., Brooks, I. M., Tjernstrom, M., Sedlar, J., Mauritsen, T., et al.
1000 (2013). Cloud and boundary layer interactions over the Arctic sea ice in late summer.
1001 *Atmospheric Chemistry and Physics*, 13, 9379-9399. https://doi.org/10.5194/acp-13-9379-2013
1002
1003 Simmonds, I. (2015). Comparing and contrasting the behaviour of Arctic and Antarctic sea ice
1004 over the 35 year period 1979-2013. *Annals of Glaciology*, 56(69), 18-28.
1005 https://doi.org/10.3189/2015AoG69A909
1006
1007 Sjöblom, A., Andersson, A., Rutgersson, A., & Falck, E. (2020). Flow over a snow-water-snow
1008 surface in the high Arctic, Svalbard: Turbulent fluxes and comparison of observation techniques.
1009 *Polar Science*, 25(100549), 1-12. https://doi.org/10.1016/j.polar.2020.100549
1010
1011 Smith, S. D., Anderson, R. J, den Hartog, G., Topham, D. R., & Perkin, R. G. (1983). An
1012 investigation of a polynya in the Canadian archipelago: 2. Structure of turbulence and sensible
1013 heat flux, *Journal of Geophysical Research: Oceans*, 88(C5), 2900-2910.
1014 https://doi.org/10.1029/JC088iC05p02900
1015

1016 Smith, S. D., Muench, R. D., & Pease, C. H. (1990). Polynyas and leads: An overview of
1017 physical processes and environment. *Journal of Geophysical Research: Oceans*, 95(C6), 9461-
1018 9479. https://doi.org/10.1029/JC095iC06p09461
1019
1020 Smith, W. L., Hansen, C., Bucholtz, A., Anderson, B. E., Beckley, M., Corbett, J., et al. (2017).
1021 Arctic-Radiation-Icebridge Sea and ice Experiment: The Arctic radiant energy system during the
1022 critical seasonal ice transition. *Bulletin of the American Meteorological Society*, 1399-1426.
1023 https://doi.org/10.1175/BAMS-D-14-00277.1
1024
1025 Sotiropoulou, G., Tjernström, M., Sedlar, J., Achtert, P., Brooks, B. J., Brooks, I. M., et al.
1026 (2016). Atmospheric conditions during the Arctic Clouds in Summer Experiment (ACSE):
1027 Contrasting open water and sea ice surfaces during melt and freeze-up seasons. *Journal of*
1028 *Climate*, 29(24), 8721-8744. https://doi.org/10.1175/JCLI-D-16-0211.1
1029
1030 Steffen, K. (1985). Warm water cells in the North Water, northern Baffin Bay during winter.
1031 *Journal of Geophysical Research: Oceans*, 90(C5), 9129-9136.
1032 https://doi.org/10.1029/JC090iC05p09129
1033
1034 Steffen, K. 1986, Ice conditions of an Arctic Polynya: North Water in winter, *Journal of*
1035 *Glaciology*, 32(112), 382-390. https://doi.org/10.3189/S0022143000012089
1036

1037 Steffen, K., & Ohmura, A. (1985). Heat exchange and surface conditions in North Water,
1038 northern Baffin Bay, *Annals of Glaciology*, 6, 178-181. https://doi.org/10.3189/1985AoG6-1-
1039 178-181
1040
1041 Tan, I., & Storelvmo, T. (2019). Evidence of strong contributions from mixed-phase clouds to
1042 Arctic climate change. *Geophysical Research Letters*, 46(5), 2894-2902.
1043 https://doi.org/10.1029/2018GL081871
1044
1045 Taylor, P. C., Kato, S., Xu, K.-M., & Cai, M. (2015). Covariance between Arctic sea ice and
1046 clouds within atmospheric state regimes at the satellite footprint level. *Journal of Geophysical*
1047 *Research: Atmospheres*, 120(24), 12656–12678. https://doi.org/10.1002/2015JD023520
1048
1049 Titchner, H. A., & Rayner, N. A. (2014). The Met Office Hadley Centre sea ice and sea surface
1050 temperature data set, version 2: 1. Sea ice concentrations. *Journal of Geophysical Research:*
1051 *Atmospheres*, 119(6), 2864-2889. https://doi.org/10.1002/2013JD020316
1052
1053 Tobo, Y., Adachi, K., DeMott, P. J., Hill, T. C. J., Hamilton, D. S., Mahowald, N. M., et al.
1054 (2019). Glacially sourced dust as a potentially significant source of ice nucleating particles.
1055 *Nature Geoscience*, 12, 253-258. https://doi.org/10.1038/s41561-019-0314-x
1056
1057 Vavrus, S. (2004). The impact of cloud feedbacks on Arctic climate under greenhouse forcing.
1058 *Journal of Climate*, 17(3), 603-615. https://doi.org/10.1175/1520-
1059 0442(2004)017<0603:TIOCFO>2.0.CO;2

Vihma, T., Pirazzini, R., Fer, I., Renfrew, I. A., Sedlar, J., Tjernström, M., et al. (2014). Advances in understanding and parameterization of small-scale physical processes in the marine Arctic climate system: A review. *Atmospheric Chemistry and Physics*, 14, 9403-9450. https://doi.org/10.5194/acp-14-9403-2014

Vincent, R. F. (2019). A study of the North Water Polynya Ice Arch using four decades of satellite data. *Scientific Reports*, 9(20278). https://doi.org/10.1038/s41598-019-56780-6

Walter, B. A. (1989). A study of the planetary boundary-layer over the polynya downwind of St. Lawrence Island in the Bering Sea using aircraft data. *Boundary-Layer Meteorology*, 48, 255-282. https://doi.org/10.1007/BF00158327

Wang, X., Key, J., Kwok, R., & Zhang, J. (2016). Comparison of Arctic sea ice thickness from satellites, aircraft, and PIOMAS data. *Remote Sensing*, *8*(9), 713. https://doi.org/10.3390/rs8090713

Weijer, W., Veneziani, M., Stössel, A., Hecht, M. W., Jeffery, N., Jonko, A., et al. (2017). Local atmospheric response to an open-ocean polynya in a high-resolution climate model. *Journal of Climate*, 30(5), 1629-1641. https://doi.org/10.1175/JCLI-D-16-0120.1

1081 Wu, D., & Lee, J. N. (2012). Arctic low cloud changes as observed by MISR and CALIOP:
1082 Implication for the enhanced autumnal warming and sea ice loss. *Journal of Geophysical*
1083 *Research: Atmospheres*, 117(D07107). https://doi.org/10.1029/2011JD017050
1084
1085 Yan, J., Jung, J., Lin, Q., Zhang, M., Xu, S., & Zhao, S. (2020). Effect of sea ice retreat on
1086 marine aerosol emissions in the Southern Ocean, Antarctica. *Science of the Total Environment*,
1087 745. https://doi.org/10.1016/j.scitotenv.2020.140773
1088
1089 Yao, T., & Tang, C. L. (2003). The formation and maintenance of the North Water Polynya.
1090 *Atmosphere-Ocean,* 41(3), 187-201. https://doi.org/10.3137/ao.410301
1091
1092 Yu, Y., Taylor, P. C., & Cai, M. (2019). Seasonal variations of Arctic low-level clouds and its
1093 linkage to sea ice seasonal variations. *Journal of Geophysical Research: Atmospheres,* 124(2),
1094 12206-12226. https://doi.org/10.1029/2019JD031014
1095
1096 Zhang, R., Wang, H., Fu, Q., Pendergrass, A. G., Wang, M., Yang, Y., et al. (2018). Local
1097 radiative feedbacks over the Arctic based on observed short-term climate variations. *Geophysical*
1098 *Research Letters*, 45(11), 5761-5770. https://doi.org/10.1029/2018GL077852
1099